Supplementary Information: Experimental amplification and squeezing of a motional state of an optically levitated nanoparticle

Martin Duchaň[1], Martin Šiler[1], Petr Jákl[1], Oto Brzobohatý[1], Andrey Rakhubovsky[2], Radim Filip[2], Pavel Zemánek[1]

[1]*Institute of Scientific Instruments of the Czech Academy of Sciences, Královopolská 147, 612 64 Brno, Czech Republic*
[2]*Department of Optics, Palacký University, 17. listopadu 1192/12, 771 46 Olomouc, Czech Republic*

Contents

S1 Classical description of transient diffusion in up-to-harmonic force fields

Let us assume a spherical particle of radius a and mass m moves in an immersion medium characterized by effective temperature T and mass normalized damping coefficient Γ, and the particle is exposed to an external force field F.

1. Constant force (e.g. gravity or static electric force)

$$F = F_\mathrm{c} = \mathrm{const.} \tag{S1}$$

A special case is the zero force which corresponds to the free diffusion and will be further referred to as the free-motion *FM*.

2. Harmonic restoring force (corresponding to a linear spring stiffness κ and a particle oscillating in a parabolic potential)

$$F = -\kappa x \equiv -m\Omega^2 x, \tag{S2}$$

where $\Omega = \sqrt{\kappa/m}$ denotes the characteristic frequency of a particle attached to the spring.

3. Destabilizing linear force (corresponding to an inverted parabolic potential *IPP*)

$$F = +\kappa_\mathrm{i} x \equiv +m\Omega_i^2 x, \tag{S3}$$

where Ω_i denotes a "frequency" corresponding to a harmonic restoring force of the stiffness $-\kappa_i$.

The above-considered options can be mutually combined but they always form a linear case regarding the nanoparticle dynamics and associated ordinary differential equations of motion.

In principle, the evolution of a single stochastic realization of the particle trajectory may be characterized by a Langevin equation [1].

$$\dot{x}(t) = v(t) \tag{S4}$$

$$\dot{v}(t) = -\Gamma v(t) + \frac{1}{m}F(x) + \eta(t), \tag{S5}$$

where $\eta(t)$ is a random process with zero mean and time covariance $\langle\eta(t)\eta(t') = \frac{2k_BT\Gamma}{m}\delta(t-t')$, where k_B is the Boltzmann constant and $\delta(t)$ is Dirac's delta function.

We aim to characterize the evolution of particle phase space probability density distribution even in cases when the initial state is not an initial point but a normally distributed phase space probability density (including non-zero correlations between position and velocity). The approach follows and extends the work of S. Chandrasekhar [?] .

The probability density function (PDF) P which corresponds to the random process obtained by the Langevin equation (S4-S5) can be obtained by solving the Fokker-Planck equation

$$\frac{\partial P}{\partial t} = -\frac{\partial}{\partial x}vP + \frac{\partial}{\partial v}\left[\Gamma v - \frac{F(x)}{m}\right]P + \Gamma\frac{k_BT}{m}\frac{\partial^2}{\partial v^2}P, \tag{S6}$$

for details see Chapter 10 of [?] . When the initial PDF at time $t = 0$ is either normal (Gaussian) or described by a point δ-function the solution of Eq. (S6) will be a Gaussian function as well, assuming the linear force profiles described above. Such a time dependent Gaussian PDF in position/velocity phase space is fully described by its mean values as elements of covariance matrix. Therefore, in the following text we will provide the explicit and exact formulas describing evolution of these 5 quantities, namely position and velocity means and their corresponding variances and a $x - v$ covariance, for the individual types of acting forces (potentials) and in different limiting cases.

[1] All over this Supplementary information we denote position x in contrast to the main part, where we use z having the same physical meaning

S1.1 Deterministic motion

For completeness, we consider here the solution of deterministic equations of motion (EM) without the stochastic term $\eta(t)$. The initial position and velocity of the particle are denoted as x_0 and v_0, respectively. Generally, the motion of a particle in phase space $\boldsymbol{x}(t) = (x(t), v(t))^T$ can be expressed as

$$\boldsymbol{x}(t) = \mathbf{U}(t)\boldsymbol{x}_0 + \boldsymbol{u}_p(t), \tag{S7}$$

where matrix $\mathbf{U}$ describes the transient time evolution from the initial phase space point and the vector $\boldsymbol{u}_p(t)$ is (when applicable) a particular solution of inhomogeneous equations of motion, e.g in the presence of the constant force F_c.

Below, we will summarize the solutions of the EM for particular cases. Figure S1 illustrates force profiles and shows the examples of solutions of equations of motion. It shows the force profiles as functions of coordinates (the first column), the time evolution in position (the second column) and velocity (3^{rd} column), and the evolution of trajectory in phase space (4^{th} column).

Free motion

$$x(t) = x_0 + v_0\frac{1}{\Gamma}\left(1 - e^{-\Gamma t}\right), \tag{S8}$$

$$v(t) = v_0 e^{-\Gamma t}. \tag{S9}$$

The particle motion is damped until it stops at $x(t \to \infty) = x_0 + \frac{v_0}{\Gamma}$.

Constant force

$$x(t) = x_0 + v_0\frac{1}{\Gamma}\left(1 - e^{-\Gamma t}\right) + \frac{F_c}{m\Gamma^2}\left(\Gamma t - 1 + e^{-\Gamma t}\right), \tag{S10}$$

$$v(t) = v_0 e^{-\Gamma t} + \frac{F_c}{m\Gamma}\left(1 - e^{-\Gamma t}\right). \tag{S11}$$

Harmonic restoring force

$$x(t) = x_0 e^{-\frac{\Gamma t}{2}}\left(\cos\omega t + \frac{\Gamma}{2\omega}\sin\omega t\right) + v_0\frac{1}{\omega}e^{-\frac{\Gamma t}{2}}\sin\omega t, \tag{S12}$$

$$v(t) = -x_0\frac{\Omega^2}{\omega}e^{-\frac{\Gamma t}{2}}\sin\omega t + v_0 e^{-\frac{\Gamma t}{2}}\left(\cos\omega t - \frac{\Gamma}{2\omega}\sin\omega t\right), \tag{S13}$$

where the oscillation frequency ω is denoted as

$$\omega = \left(\Omega^2 - \frac{\Gamma^2}{4}\right)^{\frac{1}{2}}. \tag{S14}$$

Inverted linear force

$$x(t) = x_0 e^{-\frac{\Gamma t}{2}}\left(\cosh\omega_i t + \frac{\Gamma}{2\omega_i}\sinh\omega_i t\right) + v_0\frac{1}{\omega_i}e^{-\frac{\Gamma t}{2}}\sinh\omega_i t, \tag{S15}$$

$$v(t) = x_0\frac{\Omega_i^2}{\omega_i}e^{-\frac{\Gamma t}{2}}\sinh\omega_i t + v_0 e^{-\frac{\Gamma t}{2}}\left(\cosh\omega_i t - \frac{\Gamma}{2\omega_i}\sinh\omega_i t\right), \tag{S16}$$

where ω_i denotes the "oscillation frequency" (similar to Eq. S3)

$$\omega_i = \left(\Omega_i^2 + \frac{\Gamma^2}{4}\right)^{\frac{1}{2}}. \tag{S17}$$

Harmonic restoring force with an additional constant force F_c induces a shift of the potential minimum

$$\Delta_H = \frac{F_c}{m\Omega^2} \tag{S18}$$

and gives the following solution:

$$x(t) = (x_0 - \Delta_H)\,e^{-\frac{\Gamma t}{2}}\left(\cos\omega t + \frac{\Gamma}{2\omega}\sin\omega t\right) + v_0\frac{1}{\omega}e^{-\frac{\Gamma t}{2}}\sin\omega t + \Delta_H, \tag{S19}$$

$$v(t) = -(x_0 - \Delta_H)\frac{\Omega^2}{\omega}e^{-\frac{\Gamma t}{2}}\sin\omega t + v_0 e^{-\frac{\Gamma t}{2}}\left(\cos\omega t - \frac{\Gamma}{2\omega}\sin\omega t\right), \tag{S20}$$

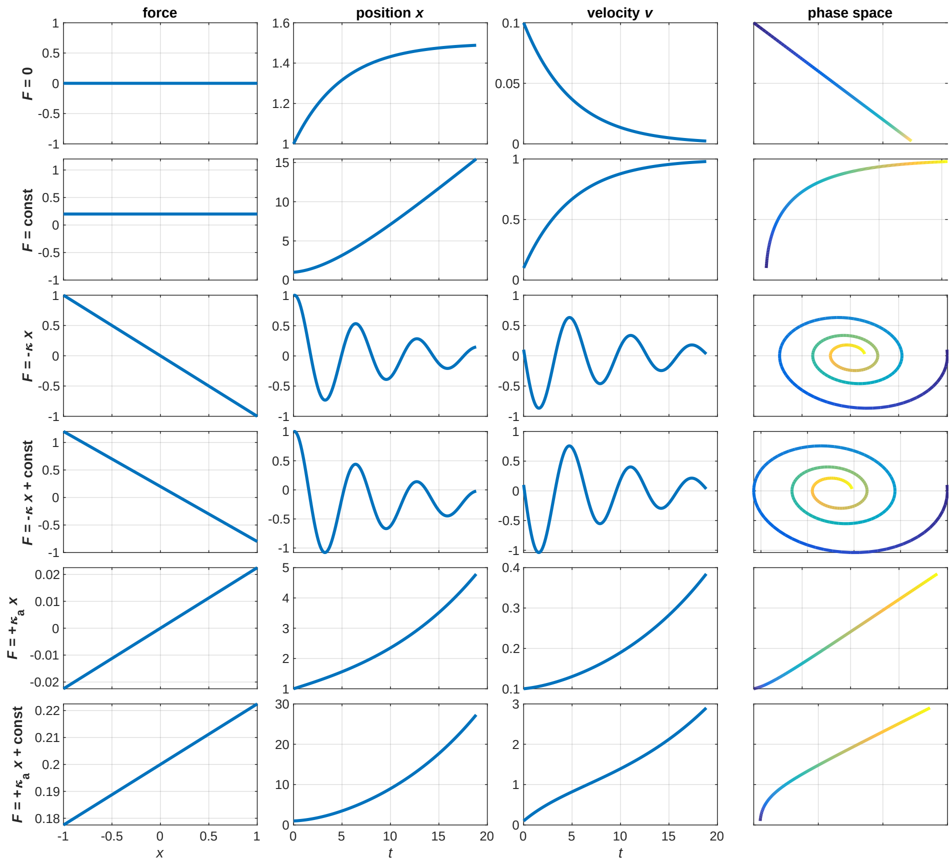

Fig. S1 | Illustration of force profiles and time evolution in position, velocity, and phase space for various considered acting forces. The color in the phase space evolution codes the time. The blue color corresponds to the initial state $t = 0$ and the color turns to yellow over time.

Inverted linear force with an additional constant force F_{c} induces a shift of the potential maximum

$$\Delta = \frac{F_{\mathrm{c}}}{m\Omega_i^2} \tag{S21}$$

with a solution

$$x(t) = (x_0 + \Delta)\,\mathrm{e}^{-\frac{\Gamma t}{2}}\left(\cosh\omega_i t + \frac{\Gamma}{2\omega_i}\sinh\omega_i t\right) + v_0\frac{1}{\omega_i}\mathrm{e}^{-\frac{\Gamma t}{2}}\sinh\omega_i t - \Delta, \tag{S22}$$

$$v(t) = (x_0 + \Delta)\,\frac{\Omega_i^2}{\omega_i}\mathrm{e}^{-\frac{\Gamma t}{2}}\sinh\omega_i t + v_0\mathrm{e}^{-\frac{\Gamma t}{2}}\left(\cosh\omega_i t - \frac{\Gamma}{2\omega_i}\sinh\omega_i t\right). \tag{S23}$$

The additional constant force F_{c} introduces just a shift in the x coordinate and taking the coordinate transformations $\tilde{x} = x + F/(m\Omega_i^2) = x + \Delta$ or $\tilde{x} = x - F/(m\Omega^2) = x - \Delta_H$ one obtains the case with zero force[?] . Therefore, these cases will not be treated below, unless required due to the analysis of the experimental data.

S1.2 Stochastic motion from a single initial point

Let us now consider that the particle motion is additionally driven by random fluctuations but all the considered realizations (trajectories) start from the same initial point in the phase space. At time $t > 0$ the phase space probability distribution (PSPD) of the particle, i.e. solution of Eq. (S6), is a Gaussian function which may be generally described in the following way[?]

$$P(\boldsymbol{x}, t|\boldsymbol{x}_0) = \frac{1}{2\pi\sqrt{\det\boldsymbol{\Theta}_{\mathrm{f}}}}\exp\left\{-\frac{1}{2}\left[\boldsymbol{x} - \mathbf{U}(t)\boldsymbol{x}_0 - \boldsymbol{u}_p(t)\right]^T\boldsymbol{\Theta}_{\mathrm{f}}^{-1}\left[\boldsymbol{x} - \mathbf{U}(t)\boldsymbol{x}_0 - \boldsymbol{u}_p(t)\right]\right\}, \tag{S24}$$

where ^{T} denotes transposition, and $\mathbf{U}(t)$ and $\boldsymbol{u}_p(t)$ are introduced in Eq. (S7) but here they describe the evolution of the mean values of particle positions. Finally, $\boldsymbol{\Theta}_\mathrm{f}$ is the time-dependent 2×2 covariance matrix

$$\boldsymbol{\Theta}_\mathrm{f}(t) = \begin{pmatrix} \theta_{\mathrm{f}xx}(t) & \theta_{\mathrm{f}xv}(t) \\ \theta_{\mathrm{f}xv}(t) & \theta_{\mathrm{f}vv}(t) \end{pmatrix} \tag{S25}$$

which is symmetric and its elements will be expressed below.

Free motion and constant force

$$\theta_{\mathrm{f}xx} = \frac{k_B T}{m\Gamma^2}\left(2\Gamma t - 3 + 4\mathrm{e}^{-\Gamma t} - \mathrm{e}^{-2\Gamma t}\right), \tag{S26}$$

$$\theta_{\mathrm{f}vv} = \frac{k_B T}{m}\left(1 - \mathrm{e}^{-2\Gamma t}\right), \tag{S27}$$

$$\theta_{\mathrm{f}xv} = \frac{k_B T}{m\Gamma}\left(1 - \mathrm{e}^{-\Gamma t}\right)^2. \tag{S28}$$

Harmonic restoring force

$$\theta_{\mathrm{f}xx} = \frac{k_B T}{m\Omega^2}\left[1 - \mathrm{e}^{-\Gamma t}\left(\frac{\Gamma^2}{2\omega^2}\sin^2\omega t + \frac{\Gamma}{2\omega}\sin 2\omega t + 1\right)\right], \tag{S29}$$

$$\theta_{\mathrm{f}vv} = \frac{k_B T}{m}\left[1 - \mathrm{e}^{-\Gamma t}\left(\frac{\Gamma^2}{2\omega^2}\sin^2\omega t - \frac{\Gamma}{2\omega}\sin 2\omega t + 1\right)\right], \tag{S30}$$

$$\theta_{\mathrm{f}xv} = \frac{k_B T}{m}\frac{\Gamma}{\omega^2}\mathrm{e}^{-\Gamma t}\sin^2\omega t. \tag{S31}$$

Inverted linear force

$$\theta_{\mathrm{f}xx} = \frac{k_B T}{m\Omega_i^2}\left[\mathrm{e}^{-\Gamma t}\left(\frac{\Gamma^2}{2\omega_i^2}\sinh^2\omega_i t + \frac{\Gamma}{2\omega_i}\sinh 2\omega_i t + 1\right) - 1\right], \tag{S32}$$

$$\theta_{\mathrm{f}vv} = \frac{k_B T}{m}\left[1 - \mathrm{e}^{-\Gamma t}\left(\frac{\Gamma^2}{2\omega_i^2}\sinh^2\omega_i t - \frac{\Gamma}{2\omega_i}\sinh 2\omega_i t + 1\right)\right], \tag{S33}$$

$$\theta_{\mathrm{f}xv} = \frac{k_B T}{m}\frac{\Gamma}{\omega_i^2}\mathrm{e}^{-\Gamma t}\sinh^2\omega_i t. \tag{S34}$$

S1.3 Stochastic motion from a normal distribution of initial points corresponding to ambient temperature T

The system starts from an initial state that is normally distributed (including correlation between x and v) in the phase space:

$$P_0(\boldsymbol{x}_0) = \frac{1}{2\pi\sqrt{\det\boldsymbol{\Theta}_0}}\exp\left\{-\frac{1}{2}\left[\boldsymbol{x}_0 - \boldsymbol{\mu}\right]^T \boldsymbol{\Theta}_0^{-1}\left[\boldsymbol{x}_0 - \boldsymbol{\mu}\right]\right\}, \tag{S35}$$

with the initial mean values $\boldsymbol{\mu} = (\mu_x, \mu_v)$ and initial covariance matrix $\boldsymbol{\Theta}_0$

$$\boldsymbol{\Theta}_0 = \begin{pmatrix} \vartheta_{xx} & \vartheta_{xv} \\ \vartheta_{xv} & \vartheta_{vv} \end{pmatrix}. \tag{S36}$$

Please note, that in the following text we will use symbols ϑ to describe the elements of the inital covariance matrix $\boldsymbol{\Theta}_0$ in time $t = 0$ while $\theta(t)$ to label the elements of covariance matrix in given time $t > 0$. The probability density for time evolution is an convolution initial position distribution with a fixed point evolution. The result of this convolution may be formally written as

$$P(\boldsymbol{x}, t|\boldsymbol{\mu}, \boldsymbol{\Theta}) = \frac{1}{2\pi\left(\det\left[\boldsymbol{\Theta}_\mathrm{f} + \mathbf{U}\boldsymbol{\Theta}_\mathbf{0}\mathbf{U}^T\right]\right)^{\frac{1}{2}}}\exp\left\{-\frac{1}{2}\left[\boldsymbol{x} - \mathbf{U}\boldsymbol{\mu} - \boldsymbol{u}_p\right]^T\left[\boldsymbol{\Theta}_\mathrm{f} + \mathbf{U}\boldsymbol{\Theta}_\mathbf{0}\mathbf{U}^T\right]^{-1}\left[\boldsymbol{x} - \mathbf{U}\boldsymbol{\mu} - \boldsymbol{u}_p\right]\right\}. \tag{S37}$$

Compared to Eq. (S24), the initial position $\boldsymbol{x}_0$ has been replaced by mean values $\boldsymbol{\mu}$ that keep evolving along the same paths as in the deterministic case. Further, the covariance matrix $\boldsymbol{\Theta}_\mathrm{f} + \mathbf{U}\boldsymbol{\Theta}_\mathbf{0}\mathbf{U}^T$ now combines the original evolution of the "thermal (diffusive)" state with the transient time dependency of the initial state (which is temperature independent). Consequently, the elements of the covariance matrix $\mathbf{\Theta} = \mathbf{\Theta}_\mathrm{f} + \mathbf{U}\mathbf{\Theta_0}\mathbf{U}^T$ can be expressed as

$$\theta_{xx} = \theta_{\mathrm{f}xx} + {U_{xx}}^2\,\vartheta_{xx} + 2\,U_{xx}\,U_{xv}\,\vartheta_{xv} + {U_{xv}}^2\,\vartheta_{vv}, \tag{S38}$$
$$\theta_{vv} = \theta_{\mathrm{f}vv} + {U_{vx}}^2\,\vartheta_{xx} + 2\,U_{vx}\,U_{vv}\,\vartheta_{xv} + {U_{vv}}^2\,\vartheta_{vv}, \tag{S39}$$
$$\theta_{xv} = \theta_{\mathrm{f}xv} + U_{xx}\,U_{vx}\,\vartheta_{xx} + (U_{xx}\,U_{vv} + U_{xv}\,U_{vx})\,\vartheta_{xv} + U_{xv}\,U_{vv}\,\vartheta_{vv} \tag{S40}$$

In the following sections, the results for particular forms of the acting forces will be expressed.

S1.3.1 Free motion

$$\langle x(t)\rangle = \mu_x + \mu_v\frac{1}{\Gamma}\left(1-\mathrm{e}^{-\Gamma t}\right), \tag{S41}$$
$$\langle v(t)\rangle = \mu_v\mathrm{e}^{-\Gamma t}, \tag{S42}$$
$$\theta_{xx}(t) = \frac{k_BT}{m\Gamma^2}\left(2\Gamma t - 3 + 4\mathrm{e}^{-\Gamma t} - \mathrm{e}^{-2\Gamma t}\right) + \vartheta_{xx} + \vartheta_{vv}\frac{1}{\Gamma^2}\left(1-\mathrm{e}^{-\Gamma t}\right)^2 + 2\vartheta_{xv}\frac{1}{\Gamma}\left(1-\mathrm{e}^{-\Gamma t}\right), \tag{S43}$$
$$\theta_{vv}(t) = \frac{k_BT}{m}\left(1-\mathrm{e}^{-2\Gamma t}\right) + \vartheta_{vv}\mathrm{e}^{-2\Gamma t}, \tag{S44}$$
$$\theta_{xv}(t) = \frac{k_BT}{m\Gamma}\left(1-\mathrm{e}^{-\Gamma t}\right)^2 + \vartheta_{vv}\frac{1}{\Gamma}\mathrm{e}^{-\Gamma t}\left(1-\mathrm{e}^{-\Gamma t}\right) + \mathrm{e}^{-\Gamma t}\vartheta_{xv}. \tag{S45}$$

Short time approximation Assuming $\Gamma t \ll 1$ and taking the leading terms in the Taylor series for particular processes one gets

$$\langle x(t)\rangle = \mu_x + \mu_v t, \tag{S46}$$
$$\langle v(t)\rangle = \mu_v\left(1-\Gamma t\right), \tag{S47}$$
$$\theta_{xx}(t) = \frac{2}{3}\frac{k_BT\Gamma}{m}t^3 + \vartheta_{xx} + \vartheta_{vv}t^2 + 2\vartheta_{xv}t, \tag{S48}$$
$$\theta_{vv}(t) = \frac{2k_BT\Gamma}{m}t + \vartheta_{vv}\left(1-\Gamma t\right), \tag{S49}$$
$$\theta_{xv}(t) = \frac{k_BT\Gamma}{m}t^2 + \vartheta_{vv}t + \vartheta_{xv}\left(1-\Gamma t\right). \tag{S50}$$

Long time limit gives for $t\to\infty$.

$$\langle x(t)\rangle = \mu_x + \frac{\mu_v}{\Gamma}, \tag{S51}$$
$$\langle v(t)\rangle = 0, \tag{S52}$$
$$\theta_{xx}(t) = \frac{2k_BT}{m\Gamma}t, \tag{S53}$$
$$\theta_{vv}(t) = \frac{k_BT}{m}, \tag{S54}$$
$$\theta_{xv}(t) = \frac{k_BT}{m\Gamma}. \tag{S55}$$

Here, we see that the particle motion is slowed down by the damping and it stops in terminal mean position $\mu_x + \frac{\mu_v}{\Gamma}$. The variance in position linearly grows following Einstein relation $\operatorname{var} x = 2Dt$, and the variance in velocity follows Maxwell's law of kinetic gas theory. The covariance of positions and velocities becomes time-independent as well but with a different rate of convergence.

S1.3.2 Constant force

$$\langle x(t)\rangle = \mu_x + \mu_v\frac{1}{\Gamma}\left(1-\mathrm{e}^{-\Gamma t}\right) + \frac{F_\mathrm{c}}{m\Gamma^2}\left(\Gamma t - 1 + \mathrm{e}^{-\Gamma t}\right), \tag{S56}$$
$$\langle v(t)\rangle = \mu_v\mathrm{e}^{-\Gamma t} + \frac{F_\mathrm{c}}{m\Gamma}\left(1-\mathrm{e}^{-\Gamma t}\right). \tag{S57}$$

The constant force keeps the covariance matrix as for the free motion expressed above.

Short time approximation

$$\langle x(t)\rangle = \mu_x + \mu_v t + \frac{1}{2}\frac{F_\mathrm{c}}{m}t^2, \tag{S58}$$

$$\langle v(t)\rangle = \mu_v\left(1-\Gamma t\right) + \frac{F_\mathrm{c}}{m}t. \tag{S59}$$

Long time limit

$$\langle x(t)\rangle = \mu_x + \frac{\mu_v}{\Gamma} + \frac{F_\mathrm{c}}{m\Gamma}t, \tag{S60}$$

$$\langle v(t)\rangle = \frac{F_\mathrm{c}}{m\Gamma}. \tag{S61}$$

The constant external force in the long time limit equilibrates with the damping which leads to constant mean particle velocity, linear grow of the mean position, and unmodified covariance matrix elements of free motion.

S1.3.3 Harmonic restoring force

$$\langle x(t)\rangle = \mu_x \mathrm{e}^{-\frac{\Gamma t}{2}}\left(\cos\omega t + \frac{\Gamma}{2\omega}\sin\omega t\right) + \mu_v\frac{1}{\omega}\mathrm{e}^{-\frac{\Gamma t}{2}}\sin\omega t, \tag{S62}$$

$$\langle v(t)\rangle = -\mu_x\frac{\Omega^2}{\omega}\mathrm{e}^{-\frac{\Gamma t}{2}}\sin\omega t + \mu_v \mathrm{e}^{-\frac{\Gamma t}{2}}\left(\cos\omega t - \frac{\Gamma}{2\omega}\sin\omega t\right), \tag{S63}$$

$$\begin{aligned}\theta_{xx}(t) = {} & \frac{k_B T}{m\Omega^2}\left[1-\mathrm{e}^{-\Gamma t}\left(\frac{\Gamma^2}{2\omega^2}\sin^2\omega t + \frac{\Gamma}{2\omega}\sin 2\omega t + 1\right)\right] \\ & +\vartheta_{xx}\mathrm{e}^{-\Gamma t}\left(\cos\omega t + \frac{\Gamma}{2\omega}\sin\omega t\right)^2 + \vartheta_{vv}\mathrm{e}^{-\Gamma t}\frac{1}{\omega^2}\sin^2\omega t \\ & +2\vartheta_{xv}\mathrm{e}^{-\Gamma t}\frac{1}{\omega}\sin\omega t\left(\cos\omega t + \frac{\Gamma}{2\omega}\sin\omega t\right),\end{aligned} \tag{S64}$$

$$\begin{aligned}\theta_{vv}(t) = {} & \frac{k_B T}{m}\left[1-\mathrm{e}^{-\Gamma t}\left(\frac{\Gamma^2}{2\omega^2}\sin^2\omega t - \frac{\Gamma}{2\omega}\sin 2\omega t + 1\right)\right], \\ & +\vartheta_{xx}\frac{\Omega^4}{\omega^2}\mathrm{e}^{-\Gamma t}\sin^2\omega t + \vartheta_{vv}\mathrm{e}^{-\Gamma t}\left(\cos\omega t - \frac{\Gamma}{2\omega}\sin\omega t\right)^2 \\ & -2\vartheta_{xv}\mathrm{e}^{-\Gamma t}\frac{\Omega^2}{\omega}\sin\omega t\left(\cos\omega t - \frac{\Gamma}{2\omega}\sin\omega t\right),\end{aligned} \tag{S65}$$

$$\begin{aligned}\theta_{xv}(t) = {} & \frac{k_B T}{m}\frac{\Gamma}{\omega^2}\mathrm{e}^{-\Gamma t}\sin^2\omega t \\ & -\vartheta_{xx}\mathrm{e}^{-\Gamma t}\frac{\Omega^2}{\omega}\sin\omega t\left(\cos\omega t + \frac{\Gamma}{2\omega}\sin\omega t\right) + \vartheta_{vv}\mathrm{e}^{-\Gamma t}\frac{1}{\omega}\sin\omega t\left(\cos\omega t - \frac{\Gamma}{2\omega}\sin\omega t\right) \\ & +\vartheta_{xv}\mathrm{e}^{-\Gamma t}\cos 2\omega t\end{aligned} \tag{S66}$$

Short time approximation assumes $\Gamma t \ll 1$ and $\Omega t \ll 1$

$$\langle x(t)\rangle = \mu_x\left[1-\frac{1}{2}(\Omega t)^2 - \frac{1}{4}(\Gamma t)^2\right] + \mu_v\left[t - \frac{1}{2}\Gamma t^2\right], \tag{S67}$$

$$\langle v(t)\rangle = -\mu_x\Omega^2\left[t-\frac{1}{2}\Gamma t^2\right] + \mu_v\left[1-\Gamma t - \frac{1}{2}(\Omega t)^2 + \frac{1}{4}(\Gamma t)^2\right] \tag{S68}$$

$$\theta_{xx}(t) = \frac{2}{3}\frac{k_B T\Gamma}{m}t^3 + \vartheta_{xx}\left[1-(\Omega t)^2\right] + \vartheta_{vv}t^2 + 2\vartheta_{xv}t \tag{S69}$$

$$\theta_{vv}(t) = \frac{2k_B T\Gamma}{m}t + \vartheta_{xx}\Omega^4 t^2 + \vartheta_{vv}\left[1-2\Gamma t - \left(\Omega^2 - 2\Gamma^2\right)t^2\right] - 2\vartheta_{xv}\Omega^2 t, \tag{S70}$$

$$\theta_{xv}(t) = \frac{k_B T\Gamma}{m}t^2 - \vartheta_{xx}\Omega^2 t + \vartheta_{vv}t + \vartheta_{xv}\left[1-\Gamma t + 2(\Omega t)^2\right]. \tag{S71}$$

Small damping approximation of harmonic oscillations assumes only $\Gamma t \ll 1$ for the Taylor series.

$$\begin{aligned}
\langle x(t)\rangle &= \mu_x \cos\Omega t + \mu_v \frac{1}{\Omega}\sin\Omega t, && \text{(S72)}\\
\langle v(t)\rangle &= -\mu_x \Omega \sin\Omega t + \mu_v \cos\Omega t && \text{(S73)}\\
\theta_{xx}(t) &= \frac{k_B T}{m\Omega^2}\Gamma t\left(1-\operatorname{sinc}2\Omega t\right) + \vartheta_{xx}\cos^2\Omega t + \vartheta_{vv}\frac{1}{\Omega^2}\sin^2\Omega t + \vartheta_{xv}\frac{1}{\Omega}\sin 2\Omega t, && \text{(S74)}\\
\theta_{vv}(t) &= \frac{k_B T}{m}\Gamma t\left(1+\operatorname{sinc}2\Omega t\right) + \vartheta_{xx}\Omega^2\sin^2\Omega t + \vartheta_{vv}\cos^2\Omega t - \vartheta_{xv}\Omega\sin 2\Omega t, && \text{(S75)}\\
\theta_{xv}(t) &= \frac{k_B T}{m}\frac{\Gamma}{\Omega^2}\sin^2\Omega t - \vartheta_{xx}\frac{1}{2}\Omega\sin 2\Omega t + \vartheta_{vv}\frac{1}{2\Omega}\sin 2\Omega t + \vartheta_{xv}\cos 2\Omega t. && \text{(S76)}
\end{aligned}$$

Long time limit

$$\begin{aligned}
\langle x(t)\rangle &= 0 && \text{(S77)}\\
\langle v(t)\rangle &= 0 && \text{(S78)}\\
\theta_{xx}(t) &= \frac{k_B T}{m\Omega^2}, && \text{(S79)}\\
\theta_{vv}(t) &= \frac{k_B T}{m}, && \text{(S80)}\\
\theta_{xv}(t) &= 0. && \text{(S81)}
\end{aligned}$$

Both the mean position and velocity of a particle in the parabolic potential converge to zero values. In contrast, the variances of position and velocity follow the equipartition theorem while their covariance also converges to zero. This means that the particle reached the thermal equilibrium state with its environment and all information about its initial state is lost.

S1.3.4 Inverted linear force

$$\begin{aligned}
\langle x(t)\rangle &= \mu_x \mathrm{e}^{-\frac{\Gamma t}{2}}\left(\cosh\omega_i t + \frac{\Gamma}{2\omega_i}\sinh\omega_i t\right) + \mu_v\frac{1}{\omega_i}\mathrm{e}^{-\frac{\Gamma t}{2}}\sinh\omega_i t, && \text{(S82)}\\
\langle v(t)\rangle &= \mu_x\frac{\Omega_i^2}{\omega_i}\mathrm{e}^{-\frac{\Gamma t}{2}}\sinh\omega_i t + \mu_v \mathrm{e}^{-\frac{\Gamma t}{2}}\left(\cosh\omega_i t - \frac{\Gamma}{2\omega_i}\sinh\omega_i t\right), && \text{(S83)}\\
\theta_{xx}(t) &= \frac{k_B T}{m\Omega_i^2}\left[\mathrm{e}^{-\Gamma t}\left(\frac{\Gamma^2}{2\omega_i^2}\sinh^2\omega_i t + \frac{\Gamma}{2\omega_i}\sinh 2\omega_i t + 1\right) - 1\right] && \\
&\quad + \vartheta_{xx}\mathrm{e}^{-\Gamma t}\left(\cosh\omega_i t + \frac{\Gamma}{2\omega_i}\sinh\omega_i t\right)^2 + \vartheta_{vv}\frac{1}{\omega_i^2}\mathrm{e}^{-\Gamma t}\sinh^2\omega_i t, && \\
&\quad + 2\vartheta_{xv}\mathrm{e}^{-\Gamma t}\frac{1}{\omega_i}\sinh\omega_i t\left(\cosh\omega_i t + \frac{\Gamma}{2\omega_i}\sinh\omega_i t\right) && \text{(S84)}\\
\theta_{vv}(t) &= \frac{k_B T}{m}\left[1 - \mathrm{e}^{-\Gamma t}\left(\frac{\Gamma^2}{2\omega_i^2}\sinh^2\omega_i t - \frac{\Gamma}{2\omega_i}\sinh 2\omega_i t + 1\right)\right] && \\
&\quad + \vartheta_{xx}\frac{\Omega_i^4}{\omega_i^2}\mathrm{e}^{-\Gamma t}\sinh^2\omega_i t + \vartheta_{vv}\mathrm{e}^{-\Gamma t}\left(\cosh\omega_i t - \frac{\Gamma}{2\omega_i}\sinh\omega_i t\right)^2 && \\
&\quad + 2\vartheta_{xv}\mathrm{e}^{-\Gamma t}\frac{\Omega_i^2}{\omega_i}\sinh\omega_i t\left(\cosh\omega_i t - \frac{\Gamma}{2\omega_i}\sinh\omega_i t\right), && \text{(S85)}\\
\theta_{xv}(t) &= \frac{k_B T}{m}\frac{\Gamma}{\omega_i^2}\mathrm{e}^{-\Gamma t}\sinh^2\omega_i t && \\
&\quad + \vartheta_{xx}\mathrm{e}^{-\Gamma t}\frac{\Omega_i^2}{\omega_i}\sinh\omega_i t\left(\cosh\omega_i t + \frac{\Gamma}{2\omega_i}\sinh\omega_i t\right) && \\
&\quad + \vartheta_{vv}\mathrm{e}^{-\Gamma t}\frac{1}{\omega_i}\sinh\omega_i t\left(\cosh\omega_i t - \frac{\Gamma}{2\omega_i}\sinh\omega_i t\right) && \\
&\quad + \vartheta_{xv}\mathrm{e}^{-\Gamma t}\left[\cosh^2\omega_i t + \left(\Omega_i^2 - \frac{\Gamma^2}{4}\right)\frac{1}{\omega_i^2}\sinh^2\omega_i t\right] && \text{(S86)}
\end{aligned}$$

Short time approximation

$$\langle x(t)\rangle = \mu_x\left[1+\frac{1}{2}(\Omega_i t)^2\right]+\mu_v\left[t-\frac{1}{2}\Gamma t^2\right], \tag{S87}$$

$$\langle v(t)\rangle = \mu_x\Omega_i^2\left[t-\frac{1}{2}\Gamma t^2\right]+\mu_v\left[1-\Gamma t-\frac{1}{2}\left(\Omega_i^2+\Gamma^2\right)t^2\right] \tag{S88}$$

$$\theta_{xx}(t) = \frac{2}{3}\frac{k_B T\Gamma}{m}t^3\left[1-\frac{\Gamma^2}{2\Omega_i^2}\right]+\vartheta_{xx}\left[1+(\Omega_i t)^2\right]+\vartheta_{vv}t^2+2\vartheta_{xv}t, \tag{S89}$$

$$\theta_{vv}(t) = \frac{2k_B T\Gamma}{m}t+\vartheta_{xx}\Omega_i^4 t^2+\vartheta_{vv}\left[1-2\Gamma t+\left(\Omega_i^2+2\Gamma^2\right)t^2\right]+2\vartheta_{xv}\Omega_i^2 t, \tag{S90}$$

$$\theta_{xv}(t) = \frac{k_B T\Gamma}{m}t^2+\vartheta_{xx}\Omega_i^2 t+\vartheta_{vv}t+\vartheta_{xv}\left[1-\Gamma t+\left(\frac{3}{2}\Omega_i^2+\frac{7}{8}\Gamma^2\right)t^2\right]. \tag{S91}$$

Long time limit assumes $\sinh\omega_i t\simeq\cosh\omega_i t\simeq\frac{1}{2}\exp(\omega_i t)$ and gives

$$\langle x(t)\rangle = \frac{1}{2}\mathrm{e}^{-\frac{\Gamma t}{2}}\mathrm{e}^{\omega_i t}\left[\mu_x\left(1+\frac{\Gamma}{2\omega_i}\right)+\mu_v\frac{1}{\omega_i}\right], \tag{S92}$$

$$\langle v(t)\rangle = \frac{1}{2}\mathrm{e}^{-\frac{\Gamma t}{2}}\mathrm{e}^{\omega_i t}\left[\mu_x\frac{\Omega_i^2}{\omega_i}+\mu_v\left(1-\frac{\Gamma}{2\omega_i}\right)\right], \tag{S93}$$

$$\theta_{xx}(t) = \frac{1}{4}\mathrm{e}^{-\Gamma t}\mathrm{e}^{2\omega_i t}\left\{\frac{k_B T}{m\Omega_i^2}\frac{\Gamma}{\omega_i}\left(1+\frac{\Gamma}{2\omega_i}\right)+\vartheta_{xx}\left(1+\frac{\Gamma}{2\omega_i}\right)^2+\vartheta_{vv}\frac{1}{\omega_i^2}+2\vartheta_{xv}\frac{\Omega_i^2}{\omega_i}\left(1+\frac{\Gamma}{2\omega_i}\right)\right\}, \tag{S94}$$

$$\theta_{vv}(t) = \frac{1}{4}\mathrm{e}^{-\Gamma t}\mathrm{e}^{2\omega_i t}\left\{\frac{k_B T}{m}\frac{\Gamma}{\omega_i}\left(1-\frac{\Gamma}{2\omega_i}\right)+\vartheta_{xx}\frac{\Omega_i^4}{\omega_i^2}+\vartheta_{vv}\left(1-\frac{\Gamma}{2\omega_i}\right)^2+2\vartheta_{xv}\frac{\Omega_i^2}{\omega_i}\left(1-\frac{\Gamma}{2\omega_i}\right)\right\}, \tag{S95}$$

$$\theta_{xv}(t) = \frac{1}{4}\mathrm{e}^{-\Gamma t}\mathrm{e}^{2\omega_i t}\left\{\frac{k_B T}{m}\frac{\Gamma}{\omega_i^2}+\vartheta_{xx}\frac{\Omega_i^2}{\omega_i}\left(1+\frac{\Gamma}{2\omega_i}\right)+\vartheta_{vv}\frac{1}{\omega_i}\left(1-\frac{\Gamma}{2\omega_i}\right)^2+2\vartheta_{xv}\left(1-\frac{\Gamma^2}{4\omega_i^2}\right)\right\}. \tag{S96}$$

We can see that the squares of the mean position and velocity as well as all elements of the covariance matrix exponentially increase in time with the same factor $\exp[(2\omega_i-\Gamma)t]$. This means, that the signal-to-noise ratio (SNR) in both position and velocity is constant and may, in principle, be larger than one.

S1.4 Normal coordinates and weak damping

S1.4.1 Normalization of coordinates

The whole process studied in this paper starts and ends with a particle moving in a parabolic potential of the same stiffness and corresponding characteristic frequency Ω_c. Therefore, it seems useful to use the initial variances corresponding to an effective initial temperature T_0, which could be different from the ambient temperature T, as the normalization factors:

$$\bar\vartheta_{xx}=\frac{m\Omega_c^2}{kT_0}\vartheta_{xx},\qquad \bar\vartheta_{vv}=\frac{m}{kT_0}\vartheta_{vv},\qquad \bar\vartheta_{xv}=\frac{m\Omega_c}{kT_0}\vartheta_{xv}, \tag{S97}$$

$$\bar\mu_x=\sqrt{\frac{m\Omega_c^2}{kT_0}}\mu_x,\qquad \bar\mu_v=\sqrt{\frac{m}{kT_0}}\mu_v. \tag{S98}$$

Similarly, the phase space coordinates can be transformed into dimensionless units $(\bar x,\bar v)$ and dimensionless time $\bar t$

$$\bar x = \sqrt{\frac{m\Omega_c^2}{kT_0}}x, \tag{S99}$$

$$\bar v = \sqrt{\frac{m}{kT_0}}v, \tag{S100}$$

$$t = \frac{1}{\Omega_c}\bar t. \tag{S101}$$

giving the normalized covariance matrix

$$\bar{\boldsymbol\Theta}=\begin{pmatrix}\bar\theta_{xx} & \bar\theta_{xv}\\ \bar\theta_{xv} & \bar\theta_{vv}\end{pmatrix}=\frac{m}{k_BT_0}\begin{pmatrix}\theta_{xx}\Omega_c^2 & \theta_{xv}\Omega_c\\ \theta_{xv}\Omega_c & \theta_{vv}\end{pmatrix}. \tag{S102}$$

S1.4.2 Characterization of the covariance ellipse

In the thermal equilibrium state corresponding to an effective temperature T_0 the covariance matrix is a unit matrix. It is therefore useful to define quantities that characterize the deviation of the state from the ideal thermal equilibrium using the characteristics of the covariance matrix. The covariance matrix uniquely defines an ellipse in the phase space having semi-axes of length $\bar{\sigma}_{\min}$, $\bar{\sigma}_{\max}$ and the angle φ between longer semi-axis $\bar{\sigma}_{\max}$ and the $\bar{x}$ axis. The length of these semi-axes is given by the covariance matrix eigenvalues

$$\bar{\sigma}^2_{\substack{\max\\ \min}} = \frac{1}{2}\left[\bar{\theta}_{xx} + \bar{\theta}_{vv} \pm \sqrt{\left(\bar{\theta}_{xx} - \bar{\theta}_{vv}\right)^2 + 4\bar{\theta}^2_{xv}}\right]. \tag{S103}$$

Except for these parameters, it is useful to consider also some other quantities

- Equivalent radius of the circle having the same radius as the ellipse, i.e.

$$\bar{\sigma}_r = \sqrt{\bar{\sigma}_{\max}\bar{\sigma}_{\min}} = \sqrt{\bar{\sigma}_{\max}\bar{\sigma}_{\min}} = \sqrt[4]{\det\bar{\mathbf{\Theta}}}. \tag{S104}$$

  where $\det\bar{\mathbf{\Theta}}$ denotes the determinant of the covariance matrix $\bar{\mathbf{\Theta}}$.

- Ellipse eccentricity

$$\bar{\epsilon} = \sqrt{1 - \frac{\bar{\sigma}^2_{\min}}{\bar{\sigma}^2_{\max}}}. \tag{S105}$$

- Squeezing coefficient [?] in units of dB as

$$\lambda_{\mathrm{sq}} = -10\log_{10}\bar{\sigma}_{\min}. \tag{S106}$$

- Excess noise

$$\delta = \bar{\sigma}_{\max} - \frac{1}{\bar{\sigma}_{\min}}. \tag{S107}$$

- Non-thermal extension

$$\eta = \frac{\bar{\sigma}_{\max} - \delta}{\bar{\sigma}_{\max}} = \frac{1}{\bar{\sigma}^2}. \tag{S108}$$

S1.4.3 Free motion

In the following paragraphs, we assume weak but not negligible damping, i.e. $\Gamma t \ll 1$, $\Gamma \ll \Omega_c$, $\Gamma \ll \Omega_i$, $\omega \simeq \Omega$, $\omega_i \simeq \Omega_i$ and we summarize the normalized forms of the time evolution of mean values and variances for the potentials expressed above. We will keep the necessary level of generality regarding the initial variances and characteristic frequencies different from the normalization one Ω_c.

$$\langle\bar{x}(\bar{t})\rangle = \bar{\mu}_x + \bar{\mu}_v\bar{t}, \tag{S109}$$

$$\langle\bar{v}(\bar{t})\rangle = \bar{\mu}_v, \tag{S110}$$

$$\bar{\theta}_{xx}(\bar{t}) = \frac{2}{3}\frac{T\Gamma}{T_0\Omega_c}\bar{t}^3 + \bar{\vartheta}_{xx} + \bar{\vartheta}_{vv}\bar{t}^2 + 2\bar{\vartheta}_{xv}\bar{t}, \tag{S111}$$

$$\bar{\theta}_{vv}(\bar{t}) = 2\frac{T\Gamma}{T_0\Omega_c}\bar{t} + \bar{\vartheta}_{vv}, \tag{S112}$$

$$\bar{\theta}_{xv}(\bar{t}) = \frac{T\Gamma}{T_0\Omega_c}\bar{t}^2 + \bar{\vartheta}_{vv}\bar{t} + \bar{\vartheta}_{xv}. \tag{S113}$$

In these normalized coordinates, it is immediately seen that the variances are enhanced by the reheating terms (proportional to Γ) that are multiplied by T/T_0. This in principle means that the re-heating process is accelerated by a factor of T/T_0 for low initial temperatures and variances grow fast in time. This could be compensated by very low Γ demanding very low experimental pressures.

S1.4.4 Constant force

$$\begin{aligned}\langle\bar{x}(\bar{t})\rangle &= \bar{\mu}_x+\bar{\mu}_v\bar{t}+\frac{1}{2}\frac{F}{\sqrt{kT_0m\Omega_c^2}}\bar{t}^2, &\text{(S114)}\\ \langle\bar{v}(\bar{t})\rangle &= \bar{\mu}_v+\frac{F}{\sqrt{kT_0m\Omega_c^2}}\bar{t}. &\text{(S115)}\end{aligned}$$

The covariance matrix elements are the same as in free motion.

S1.4.5 Harmonic restoring force

$$\begin{aligned}\langle\bar{x}(\bar{t})\rangle &= \bar{\mu}_x\cos\frac{\Omega}{\Omega_c}\bar{t}+\bar{\mu}_v\frac{\Omega_c}{\Omega}\sin\frac{\Omega}{\Omega_c}\bar{t}, &\text{(S116)}\\ \langle\bar{v}(\bar{t})\rangle &= -\bar{\mu}_x\frac{\Omega}{\Omega_c}\sin\frac{\Omega}{\Omega_c}\bar{t}+\bar{\mu}_v\cos\frac{\Omega}{\Omega_c}\bar{t}, &\text{(S117)}\\ \bar{\theta}_{xx}(\bar{t}) &= \frac{T\Gamma}{T_0\Omega_c}\bar{t}\,\frac{\Omega_c^2}{\Omega^2}\left[1-\operatorname{sinc}2\frac{\Omega}{\Omega_c}\bar{t}\right]+\bar{\vartheta}_{xx}\cos^2\frac{\Omega}{\Omega_c}\bar{t}+\bar{\vartheta}_{vv}\frac{\Omega_c^2}{\Omega^2}\sin^2\frac{\Omega}{\Omega_c}\bar{t}+\bar{\vartheta}_{xv}\frac{\Omega_c}{\Omega}\sin2\frac{\Omega}{\Omega_c}\bar{t}, &\text{(S118)}\\ \bar{\theta}_{vv}(\bar{t}) &= \frac{T\Gamma}{T_0\Omega_c}\bar{t}\left[1+\operatorname{sinc}2\frac{\Omega}{\Omega_c}\bar{t}\right]+\bar{\vartheta}_{xx}\frac{\Omega^2}{\Omega_c^2}\sin^2\frac{\Omega}{\Omega_c}\bar{t}+\bar{\vartheta}_{vv}\cos^2\frac{\Omega}{\Omega_c}\bar{t}-\bar{\vartheta}_{xv}\frac{\Omega}{\Omega_c}\sin2\frac{\Omega}{\Omega_c}\bar{t}, &\text{(S119)}\\ \bar{\theta}_{xv}(\bar{t}) &= \frac{T\Gamma}{T_0\Omega_c}\frac{\Omega_c^2}{\Omega^2}\sin^2\frac{\Omega}{\Omega_c}\bar{t}+\frac{1}{2}\left[-\bar{\vartheta}_{xx}\frac{\Omega}{\Omega_c}+\bar{\vartheta}_{vv}\frac{\Omega_c}{\Omega}\right]\sin2\frac{\Omega}{\Omega_c}\bar{t}+\bar{\vartheta}_{xv}\cos2\frac{\Omega}{\Omega_c}\bar{t}. &\text{(S120)}\end{aligned}$$

where Ω denotes the characteristic frequency which can be different from the normalization one Ω_c.

However, if we assume $\Omega_c\equiv\Omega$, the eigenvalues of the covariance matrix $\lambda_{\substack{\max\\ \min}}$ have a compact form

$$\begin{aligned}\lambda_{\substack{\max\\ \min}}\equiv\bar{\sigma}^2_{\substack{\max\\ \min}} &= \frac{T\Gamma}{T_0\Omega_c}\bar{t}+\frac{\bar{\vartheta}_{xx}+\bar{\vartheta}_{vv}}{2}\\ &\pm\frac{1}{2}\sqrt{\left(\bar{\vartheta}_{xx}-\bar{\vartheta}_{vv}\right)^2+4\bar{\vartheta}_{xv}^2+4\frac{T\Gamma}{T_0\Omega_c}\left(\frac{T\Gamma}{T_0\Omega_c}-2\bar{\vartheta}_{xv}\right)\sin^2\bar{t}-2\frac{T\Gamma}{T_0\Omega_c}\left(\bar{\vartheta}_{xx}-\bar{\vartheta}_{vv}\right)\sin2\bar{t}}. \quad \text{(S121)}\end{aligned}$$

where, in accordance with the main text and Section S1.4.2, we denoted the lengths of the major and minor semiaxes of the phase space probability distribution as $\sigma_{\substack{\max\\ \min}}$.

It is seen that the reheating term $T\Gamma/(T_0\Omega_c)$ is responsible for the variation of the semiaxes lengths in time. Both eigenvalues λ grow linearly in time in combination with their oscillations at $2\Omega_c$.

If damping Γ can be neglected, one gets

$$\lambda_{\substack{\max\\ \min}}=\frac{1}{2}\left[\bar{\vartheta}_{xx}+\bar{\vartheta}_{vv}\pm\sqrt{\left(\bar{\vartheta}_{xx}-\bar{\vartheta}_{vv}\right)^2+4\bar{\vartheta}_{xv}^2}\right]. \quad \text{(S122)}$$

where the covariance matrix ellipse just rotates in space but does not change its shape.

Therefore, from the behavior of the covariance matrix in time one can estimate the initial variances.

S1.4.6 Inverted linear force

$$\begin{aligned}\langle\bar{x}(\bar{t})\rangle &= \bar{\mu}_x\cosh\frac{\Omega_i}{\Omega_c}\bar{t}+\bar{\mu}_v\frac{\Omega_c}{\Omega_i}\sinh\frac{\Omega_i}{\Omega_c}\bar{t}, &\text{(S123)}\\ \langle\bar{v}(\bar{t})\rangle &= \bar{\mu}_x\frac{\Omega_i}{\Omega_c}\sinh\frac{\Omega_i}{\Omega_c}\bar{t}+\bar{\mu}_v\cosh\frac{\Omega_i}{\Omega_c}\bar{t}, &\text{(S124)}\\ \bar{\theta}_{xx}(\bar{t}) &= \frac{T\Gamma}{T_0\Omega_c}\bar{t}\,\frac{\Omega_c^2}{\Omega_i^2}\left[\frac{\Omega_c}{2\Omega_i\bar{t}}\sinh2\frac{\Omega_i}{\Omega_c}\bar{t}-1\right]+\bar{\vartheta}_{xx}\cosh^2\frac{\Omega}{\Omega_c}\bar{t}+\bar{\vartheta}_{vv}\frac{\Omega_c^2}{\Omega^2}\sinh^2\frac{\Omega}{\Omega_c}\bar{t}+\bar{\vartheta}_{xv}\frac{\Omega_c}{\Omega}\sinh2\frac{\Omega}{\Omega_c}\bar{t}, &\text{(S125)}\\ \bar{\theta}_{vv}(\bar{t}) &= \frac{T\Gamma}{T_0\Omega_c}\bar{t}\left[1+\frac{\Omega_c}{2\Omega_i\bar{t}}\sinh2\frac{\Omega}{\Omega_c}\bar{t}\right]+\bar{\vartheta}_{xx}\frac{\Omega_i^2}{\Omega_c^2}\sinh^2\frac{\Omega_i}{\Omega_c}\bar{t}+\bar{\vartheta}_{vv}\cosh^2\frac{\Omega_i}{\Omega_c}\bar{t}+\bar{\vartheta}_{xv}\frac{\Omega_i}{\Omega_c}\sinh2\frac{\Omega_i}{\Omega_c}\bar{t}, &\text{(S126)}\\ \bar{\theta}_{xv}(\bar{t}) &= \frac{T\Gamma}{T_0\Omega_c}\frac{\Omega_c^2}{\Omega_i^2}\sinh^2\frac{\Omega_i}{\Omega_c}\bar{t}+\frac{1}{2}\left[\bar{\vartheta}_{xx}\frac{\Omega_i}{\Omega_c}+\bar{\vartheta}_{vv}\frac{\Omega_c}{\Omega_i}\right]\sinh2\frac{\Omega_i}{\Omega_c}\bar{t}+\bar{\vartheta}_{xv}\cosh2\frac{\Omega_i}{\Omega_c}\bar{t}. &\text{(S127)}\end{aligned}$$

S1.4.7 Inverted linear force with an additional constant force

Let us now assume the additional constant force F_c acts in combination with the inverted harmonic force. It corresponds to the normalized offset $\bar{\Delta}_c$ of the potential maximum

$$\bar{\Delta}_c = \frac{F_c}{\sqrt{m\Omega_c^2 k_B T_0}}, \tag{S128}$$

which is again given with respect to characteristic frequency and initial state temperature. The phase space mean displacement in position and velocity is then given as

$$\begin{aligned} \langle\bar{x}(\bar{t})\rangle &= \left(\bar{\mu}_x + \bar{\Delta}_c\right)\cosh\frac{\Omega_i}{\Omega_c}\bar{t} + \bar{\mu}_v\frac{\Omega_c}{\Omega_i}\sinh\frac{\Omega_i}{\Omega_c}\bar{t} - \bar{\Delta}_c, &\text{(S129)}\\ \langle\bar{v}(\bar{t})\rangle &= \left(\bar{\mu}_x + \bar{\Delta}_c\right)\frac{\Omega_i}{\Omega_c}\sinh\frac{\Omega_i}{\Omega_c}\bar{t} + \bar{\mu}_v\cosh\frac{\Omega_i}{\Omega_c}\bar{t}. &\text{(S130)}\end{aligned}$$

S1.5 Energy gain during a short pulse

Let us consider the initial state corresponds to an equilibrium state in a parabolic potential with characteristic frequency Ω_c and the effective temperature T_0, which may differ from the ambient temperature T. This means, that in normal coordinates, the initial state can be characterized by $\bar{\mu}_x = \bar{\mu}_v = 0$, $\bar{\vartheta}_{xx} = \bar{\vartheta}_{vv} = 1$, and $\bar{\vartheta}_{xv} = 0$. At time $\bar{t} = 0$ the parabolic potential is abruptly switched to a different one (either free motion, parabolic potential with a different characteristic frequency, or inverted parabolic potential) and after a certain duration $\bar{\tau}$ the initial parabolic potential is restored. In this section, the energy of a particle in the restored parabolic potential is analyzed so that one could quantify the energy state of the system.

The energy of the particle in the restored parabolic potential (harmonic oscillator) can be expressed as

$$\begin{aligned} \langle E\rangle &= \frac{1}{2}m\Omega_c^2\langle x^2\rangle + \frac{1}{2}m\langle v^2\rangle \\ &= \frac{1}{2}m\Omega_c^2\left(\langle x\rangle^2 + \theta_{xx}\right) + \frac{1}{2}m\left(\langle v\rangle^2 + \theta_{vv}\right) \end{aligned} \tag{S131}$$

which in the normal coordinates equals to

$$\langle\bar{E}\rangle = \frac{1}{2}\left[\langle\bar{x}\rangle^2 + \langle\bar{v}\rangle^2 + \bar{\theta}_{xx} + \bar{\theta}_{vv}\right] \tag{S132}$$

Since the mean values and covariances are expressed above for various types of interactions during the pulse $\bar{\tau}$, this equation can be used to express the particle energy for the following particular cases.

S1.5.1 Free motion

$$\langle\bar{E}\rangle = 1 + \frac{T\Gamma}{T_0\Omega_c}\bar{\tau}\left(1 + \frac{1}{3}\bar{\tau}^2\right) + \frac{1}{2}\bar{\tau}^2. \tag{S133}$$

Here, the first term corresponds to the potential and kinetic energy of the initial state, the second term corresponds to the increase of kinetic (linear with pulse duration) and potential (quartic with pulse duration) energies due to reheating. Finally, the last term corresponds to the potential energy gained by the extension of position (squeezing) during the free motion.

S1.5.2 Constant force

$$\langle\bar{E}\rangle = 1 + \frac{T\Gamma}{T_0\Omega_c}\bar{\tau}\left(1 + \frac{1}{3}\bar{\tau}^2\right) + \frac{1}{2}\bar{\tau}^2 + \frac{1}{2}\bar{\Delta}_c^2\bar{\tau}^2\left(1 + \frac{1}{4}\bar{\tau}^2\right), \tag{S134}$$

where $\bar{\Delta}_c^2$ is effective force offset given by Eq. (S128). The constant force contributed both to the kinetic ($\sim\bar{\tau}^2$) as well as to the potential energy ($\sim\bar{\tau}^4$).

S1.5.3 Harmonic restoring force

In order to distinguish frequencies of the harmonic oscillator before/after the pulse and during the pulse we will further denote the frequency during the pulse as Ω_p. Energy after the pulse is then

$$\langle\bar{E}\rangle = \frac{1}{2}\left\{\frac{T\Gamma}{T_0\Omega_c}\bar{\tau}\left[1 + \frac{\Omega_c^2}{\Omega_p^2}\right] + \frac{T\Gamma}{T_0\Omega_c}\left[1 - \frac{\Omega_c^2}{\Omega_p^2}\right]\frac{\Omega_c}{2\Omega_p}\sin\frac{2\Omega_p\bar{\tau}}{\Omega_c} + 2\cos^2\frac{\Omega_p\bar{\tau}}{\Omega_c} + \left[\frac{\Omega_c^2}{\Omega_p^2} + \frac{\Omega_p^2}{\Omega_c^2}\right]\sin^2\frac{\Omega_p\bar{\tau}}{\Omega_c}\right\}. \tag{S135}$$

Assuming short pulse, i.e. $\Omega_p\bar{\tau}/\Omega_c \ll 1$ the expansion to the Taylor series gives

$$\langle \bar{E}\rangle = 1 + \frac{T\Gamma}{T_0\Omega_c}\bar{\tau} + \frac{1}{2}\bar{\tau}^2\left[1 - \frac{\Omega_p^2}{\Omega_c^2}\right]^2. \tag{S136}$$

S1.5.4 Inverted linear force

$$\langle \bar{E}\rangle = \frac{1}{2}\left\{\frac{T\Gamma}{T_0\Omega_c}\bar{\tau}\left[1 - \frac{\Omega_c^2}{\Omega_i^2}\right] + \frac{T\Gamma}{T_0\Omega_c}\left[1 + \frac{\Omega_c^2}{\Omega_i^2}\right]\frac{\Omega_c}{2\Omega_i}\sinh\frac{2\Omega_i\bar{\tau}}{\Omega_c} + 2\cosh^2\frac{\Omega_i\bar{\tau}}{\Omega_c} + \left[\frac{\Omega_c^2}{\Omega_i^2} + \frac{\Omega_i^2}{\Omega_c^2}\right]\sinh^2\frac{\Omega_i\bar{\tau}}{\Omega_c}\right\}, \tag{S137}$$

ans similarly as above the Taylor series for short pulse ($\Omega_i\bar{\tau}/\Omega_c \ll 1$) gives

$$\bar{E} = 1 + \frac{T\Gamma}{T_0\Omega_c}\bar{\tau} + \frac{1}{2}\bar{\tau}^2\left[1 + \frac{\Omega_i^2}{\Omega_c^2}\right]^2. \tag{S138}$$

S1.5.5 Inverted linear force with an additional constant force

The energy can be expressed as the sum of two terms

$$\langle E\rangle = \langle E_i\rangle + \langle E_p\rangle, \tag{S139}$$

where E_i is the energy corresponding to the zero additional force (i.e. zero mutual shift Δ (Eq. (S21)) of the maximum of the inverted parabolic potential and minimum of the parabolic potential) given by Eq. (S138) and the energy E_p caused by the external force F_c

$$\begin{aligned}\langle E_p\rangle &= \frac{F_c^2}{2m\Omega_i^2}\left\{\frac{\Omega_c^2}{\Omega_i^2}\left[\cosh\frac{\Omega_i\bar{\tau}}{\Omega_c} - 1\right]^2 + \sinh^2\frac{\Omega_i\bar{\tau}}{\Omega_c}\right\}\\ &= \frac{1}{2}m\Omega_i^2\Delta^2\left\{\frac{\Omega_c^2}{\Omega_i^2}\left[\cosh\frac{\Omega_i\bar{\tau}}{\Omega_c} - 1\right]^2 + \sinh^2\frac{\Omega_i\bar{\tau}}{\Omega_c}\right\}\\ &\approx \frac{F_c^2}{2m\Omega_c^2}\bar{\tau}^2\left(1 + \frac{1}{4}\bar{\tau}^2\right).\end{aligned} \tag{S140}$$

The energy E_p in normal coordinates may be expressed as

$$\langle \bar{E}_p\rangle = \frac{1}{2}\bar{\Delta}_c^2\left\{\left[\cosh\frac{\Omega_i\bar{\tau}}{\Omega_c} - 1\right]^2 + \frac{\Omega_i^2}{\Omega_c^2}\sinh^2\frac{\Omega_i\bar{\tau}}{\Omega_c}\right\}, \tag{S141}$$

where $\bar{\Delta}_c$ is the normal coordinates force offset calculated given by Eq. (S128).

S1.6 Second order coherence

The classical definition of the second order coherence $g^{(2)}$ comes from the theory of light coherence:

$$g^{(2)}(t_1, \mathbf{r}_1, t_2, \mathbf{r}_2) = \frac{\langle I(\mathbf{r}_1, t_1)I(\mathbf{r}_2, t_2)\rangle}{\langle I(\mathbf{r}_1, t_1)\rangle\langle I(\mathbf{r}_2, t_2)\rangle}. \tag{S142}$$

where $I(\mathbf{r}, t)$ denote the optical intensity of light at particular position $\mathbf{r}$ and time t, $\langle\rangle$ here denotes the averages over statistical ensembles as we do not assume the stationary states.

In order to quantify the coherence of the optomechanicaly squeezed Gaussian states we first use the state energy $\bar{E}$ instead of light intensity, where

$$\bar{E}(t) = \frac{1}{2}\left[\bar{x}(t)^2 + \bar{v}(t)^2\right]. \tag{S143}$$

In stationary states the dependence on both times t_1, t_2 is replaced by a time delay τ_g between the first and second state. The value of $g^{(2)}$ for zero time delay $\tau_g = 0$ is then used to quantify the state of light coherence, e.g. $g^{(2)} = 1$ or $g^{(2)} = 2$ correspond to the single frequency or thermal light. Similarly, we will quantify the coherence of the non-stationary states by the second order coefficient given at the same time, i.e.

$$g^{(2)}(t, t) = \frac{\langle E(t)^2\rangle}{\langle E(t)\rangle^2}. \tag{S144}$$

Further, let us assume the state at the given time has zero mean and covariance matrix $\mathbf{\Theta}$. For such a state the coherence coefficient may be expressed directly using the elements of $\mathbf{\Theta}$ as

$$g^{(2)}(t,t) = \frac{3\theta_{xx}^2 + 2\theta_{xx}\theta_{vv} + 3\theta_{vv}^2 + 4\theta_{xv}^2}{\theta_{xx}^2 + 2\theta_{xx}\theta_{vv} + \theta_{vv}^2}. \tag{S145}$$

Assuming initial thermal-like state with initial temperature T_0, i.e. $\vartheta_{xx} = \vartheta_{vv} = 1$, $\vartheta_{xv} = 0$ and negligible damping we may derive a simple relation for $g^{(2)}(t,t)$ for free motion

$$g^{(2)}_{\mathrm{FM}}(\bar{t},\bar{t}) = \frac{8 + 12\bar{t}^2 + 3\bar{t}^4}{4 + 4\bar{t}^2 + \bar{t}^4}. \tag{S146}$$

One gets $g^{(2)}_{\mathrm{FF}}(0,0) = 2$ which confirms the initial state corresponds to the thermal state. In contrast in the long time limit, one can get for the free motion or inverted parabolic potential

$$\lim_{\bar{t}\to\infty} g^{(2)}_{\mathrm{IPP,FM}}(\bar{t},\bar{t}) = 3. \tag{S147}$$

This implies that the nonequilibrium optomechanical states correspond to the super bunched state considering the coherence point of view. Let us stress, Eq. (S147) is valid only in states with zero means.

When an offset is present (especially in the IPP case) the energy of the state would contain a significant contribution from the mean values. This would enhance the denominator in Eq. (S144) and, in principle, the state may become close to the coherent one (having $1 < g^{(2)}(t,t) < 2$) instead of the super bunched one.

S1.7 Optomechanical initial state amplification

In this section, we will focus on an evolution of the mean particle position and velocity before, during, and after a short pulse of various force profiles discussed above. Namely, we will consider the evolution of mean values of the phase space position in a three-step sequence shown in Fig. 1 of the main text.

The initial state is given by the mean particle phase space position (μ_x, μ_v) and Gaussian distributed with initial variances $\vartheta_{xx}, \vartheta_{vv}, \vartheta_{xv}$ corresponding to an effective initial temperature T_0.

1. The particle evolves from the initial state in a parabolic potential of characteristic frequency Ω_c. The evolution of the probability density in the phase space is given by a pure rotation which is defined by the duration of this step I $\bar{\tau}_1$.

2. At $\bar{\tau}_1$ the force field is abruptly switched. The free motion occurs is the parabolic potential is switched off and no other force acts on the particle. Weak parabolic potential (WPP) occurs if the new parabolic potential has smaller stiffness and the characteristic frequency Ω_p. In principle the potential strength may be increased as well, i.e. $\Omega_p > \Omega_c$. However, we will denote this case as WPP as well. Alternativelly, the inverted parabolic potential (IPP) occurs if the parabolic potential is switched off and the inverted is switched on with a corresponding frequency Ω_i. The duration of this pulse is $\bar{\tau}_2$.

3. The original parabolic potential with Ω_c is restored and the particle evolves here for a period $\bar{\tau}_3$. At the end of the period its state could verified if the system is in the quantum regime and just a single measurement is allowed.

The following phase space vectors will be further used to describe the initial conditions $\mathbf{x}_0 = (\langle\bar{x}(0)\rangle, \langle\bar{v}(0)\rangle)^T = (\bar{\mu}_x, \bar{\mu}_v)^T$, state at the start of the force pulse $\mathbf{x}_1 = (\langle\bar{x}(\bar{\tau}_1)\rangle, \langle\bar{v}(\bar{\tau}_1)\rangle)^T$, after force pulse $\mathbf{x}_2 = (\langle\bar{x}(\bar{\tau}_1+\bar{\tau}_2)\rangle, \langle\bar{v}(\bar{\tau}_1+\bar{\tau}_2)\rangle)^T$, and the final phase space position $\mathbf{x}_F = (\langle\bar{x}(\bar{\tau}_1+\bar{\tau}_2+\bar{\tau}_3)\rangle, \langle\bar{v}(\bar{\tau}_1+\bar{\tau}_2+\bar{\tau}_3)\rangle)^T$. The whole three-step sequence of harmonic-pulse-harmonic evolution may be formally written as a linear transformation

$$\mathbf{x}_F = \mathbf{R}_3\mathbf{P}\mathbf{R}_1\mathbf{x}_0, \tag{S148}$$

with $\mathbf{R}_1$ and $\mathbf{R}_3$ are matrices describing rotation in harmonic restoring force and matrix $\mathbf{P}$ describes the effect of force pulse.

Let us firstly focus on the change of the mean values of position and velocity caused by the force pulse of different types and relate the phase space vectors immediately before and after the pulse:

$$\mathbf{x}_2 = \mathbf{P}\mathbf{x}_1 = \begin{pmatrix} \mathcal{A} & \mathcal{P}\mathcal{B} \\ \frac{1}{\mathcal{P}'}\mathcal{B} & \mathcal{A} \end{pmatrix}\mathbf{x}_1 \tag{S149}$$

where $\mathcal{A}$, $\mathcal{B}$, $\mathcal{P}$, and $\mathcal{P}'$ depend on the force acting during the pulse, its duration and the characteristic frequency Ω_c and are given as follows

	Free motion	Parabolic potential	Inverted parabolic potential
$\mathcal{A}$	1	$\cos\frac{\Omega_p}{\Omega_c}\bar{\tau}_2$	$\cosh\frac{\Omega_i}{\Omega_c}\bar{\tau}_2$
$\mathcal{B}$	$\bar{\tau}_2$	$\sin\frac{\Omega_p}{\Omega_c}\bar{\tau}_2$	$\sinh\frac{\Omega_i}{\Omega_c}\bar{\tau}_2$
$\mathcal{P}$	1	$\frac{\Omega_c}{\Omega_p}$	$\frac{\Omega_c}{\Omega_i}$
$\mathcal{P}'$	$\frac{1}{\mathcal{P}'}=0$	$-\mathcal{P}$	$\mathcal{P}$

(S150)

The determinant of the pulse transitional matrix $\mathbf{P}$ in Eq. (S149) with elements given in Eq. (S150) equals to 1. This means that $\mathbf{P}$ is a symplectic matrix that can be by means of "Bloch-Messiah" decomposition**?** expressed as

$$\mathbf{P} = \mathbf{S}_3\mathbf{G}\mathbf{S}_1 = \begin{pmatrix} \cos\phi_3 & -\sin\phi_3 \\ \sin\phi_3 & \cos\phi_3 \end{pmatrix}\begin{pmatrix} G & 0 \\ 0 & G^{-1} \end{pmatrix}\begin{pmatrix} \cos\phi_1 & -\sin\phi_1 \\ \sin\phi_1 & \cos\phi_1 \end{pmatrix}, \tag{S151}$$

where $\mathbf{S}_1$, and $\mathbf{S}_3$ are orthonormal symplectic matrices that can be equivalently described as rotations by certain angles ϕ_1, and ϕ_3, and $\mathbf{G}$ is diagonal scale matrix which amplifies one coordinate by a factor G while compressing the other by a factor G^{-1}. Left and right multiplications of Eq. (S151) by inverted (i.e. transposed) matrices $\mathbf{S}_1$, and $\mathbf{S}_3$ lead to

$$\mathbf{G} = \mathbf{S}_3^T\mathbf{P}\mathbf{S}_1^T. \tag{S152}$$

This means that the three-step sequence of particle evolution can be written as

$$\mathbf{x}_F = \mathbf{R}_3\mathbf{P}\mathbf{R}_1\mathbf{x}_0 = \mathbf{G}\mathbf{x}_0, \qquad \text{when } \mathbf{R}_1 \equiv \mathbf{S}_1^T \text{ and } \mathbf{R}_3 \equiv \mathbf{S}_3^T, \tag{S153}$$

i.e.

$$x_F = Gx_0, \tag{S154}$$

$$v_F = \frac{1}{G}v_0. \tag{S155}$$

In order to fulfill this transformation the duration of evolution in harmonic potential has to be equal to angles obtained by "Bloch-Messiah" decomposition**?** ($\bar{\tau}_1 = \phi_1$ and $\bar{\tau}_3 = \phi_3$). Both times $\bar{\tau}_1$ and $\bar{\tau}_3$ can be found by putting the off-diagonal terms of $\mathbf{R}_3\mathbf{P}\mathbf{R}_1$ to 0. Their values and corresponding G given by

$$\bar{\tau}_1 = -\frac{\pi}{4} - \frac{1}{2}\operatorname{atan}\Psi + k\frac{\pi}{2}, \qquad \bar{\tau}_1' = \frac{\pi}{4} - \frac{1}{2}\operatorname{atan}\Psi + k\frac{\pi}{2}, \tag{S156}$$

$$\bar{\tau}_3 = \frac{\pi}{4} - \frac{1}{2}\operatorname{atan}\Psi + k\frac{\pi}{2} + 2l\pi, \qquad \bar{\tau}_3' = -\frac{\pi}{4} - \frac{1}{2}\operatorname{atan}\Psi + k\frac{\pi}{2} + 2l\pi, \tag{S157}$$

$$G = \mathcal{G} + (-1)^k\mathcal{A}\sqrt{1+\Psi^2}, \qquad G' = -\mathcal{G} + (-1)^k\mathcal{A}\sqrt{1+\Psi^2}, \tag{S158}$$

where

$$\Psi = \frac{\mathcal{B}}{2\mathcal{A}}\left(\mathcal{P} - \frac{1}{\mathcal{P}'}\right), \qquad \mathcal{G} = \frac{B}{2}\left(\mathcal{P} + \frac{1}{\mathcal{P}'}\right), \tag{S159}$$

k and l are integer numbers and ($\bar{\tau}_1$, $\bar{\tau}_3$, G) and ($\bar{\tau}_1'$, $\bar{\tau}_3'$, G') are 2 complementary sets of solutions, that satisfy the following equalities

$$GG' = 1, \qquad \bar{\tau}_1 + \bar{\tau}_3 = \bar{\tau}_1' + \bar{\tau}_3'. \tag{S160}$$

It is worth to stress that the two solutions of G for even and odd k satisfy $|G(k_{\text{odd}})| = 1/|G(k_{\text{even}})|$. Proper selection of k thus determines if the amplifier will amplify position or velocity but the maximal value of $|G|$ does not depend on k for given τ_2.

The factors $\Psi = \frac{\mathcal{B}}{2\mathcal{A}}\left(\mathcal{P} - \frac{1}{\mathcal{P}'}\right)$ and $\mathcal{G} = \frac{\mathcal{B}}{2}\left(\mathcal{P} + \frac{1}{\mathcal{P}'}\right)$ taking place in equations above are for each pulse type given as

	Free motion	Parabolic potential	Inverted parabolic potential
$\Psi = \frac{\mathcal{B}}{2\mathcal{A}}\left(\mathcal{P} - \frac{1}{\mathcal{P}'}\right)$	$\frac{1}{2}\bar{\tau}_2$	$\frac{1}{2}\left(\frac{\Omega_c}{\Omega_p} + \frac{\Omega_p}{\Omega_c}\right)\tan\frac{\Omega_p}{\Omega_c}\bar{\tau}_2$	$\frac{1}{2}\left(\frac{\Omega_c}{\Omega_i} - \frac{\Omega_i}{\Omega_c}\right)\tanh\frac{\Omega_i}{\Omega_c}\bar{\tau}_2$
$\mathcal{G} = \frac{\mathcal{B}}{2}\left(\mathcal{P} + \frac{1}{\mathcal{P}'}\right)$	$\frac{1}{2}\bar{\tau}_2$	$\frac{1}{2}\left(\frac{\Omega_c}{\Omega_p} - \frac{\Omega_p}{\Omega_c}\right)\sin\frac{\Omega_p}{\Omega_c}\bar{\tau}_2$	$\frac{1}{2}\left(\frac{\Omega_c}{\Omega_i} + \frac{\Omega_i}{\Omega_c}\right)\sinh\frac{\Omega_i}{\Omega_c}\bar{\tau}_2$

(S161)

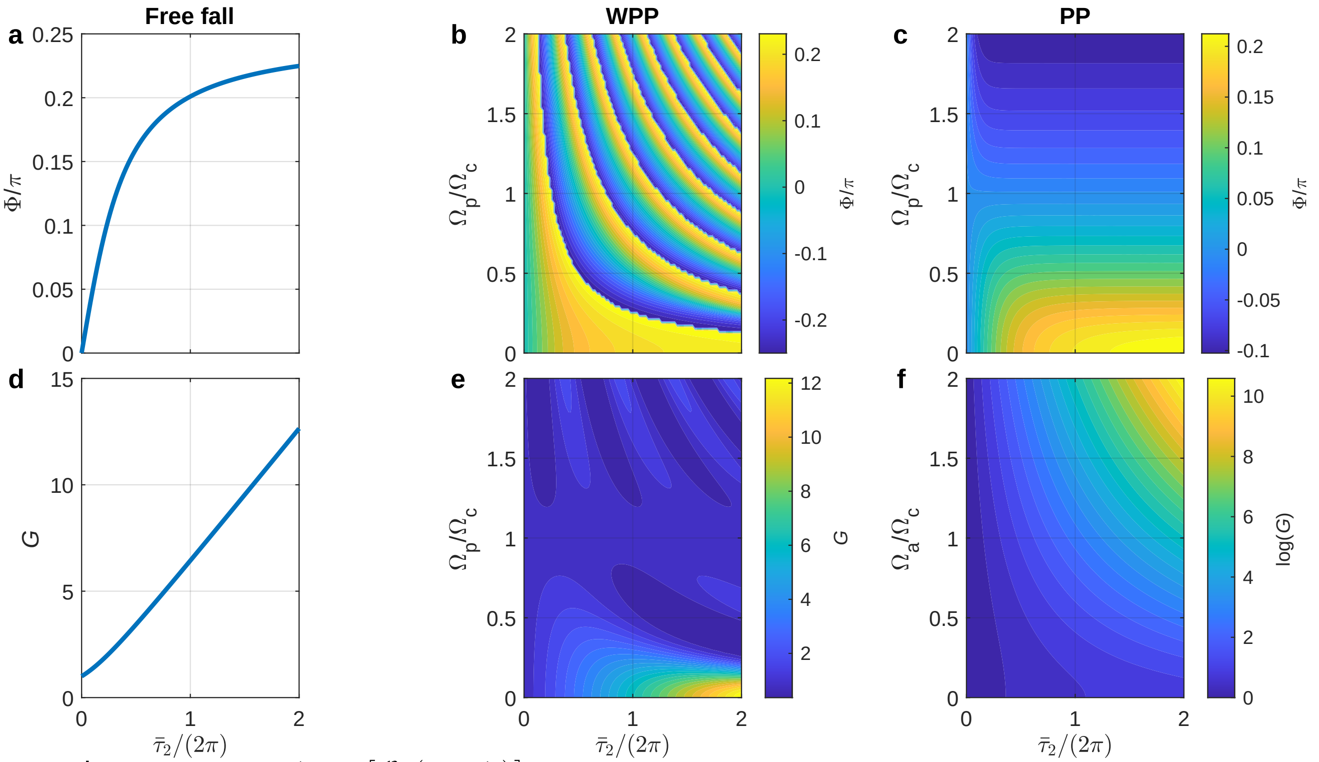

Fig. S2 | The angle $\Phi = \frac{1}{2}\,\mathrm{atan}\left[\frac{\mathcal{B}}{2\mathcal{A}}\left(\mathcal{P} - \frac{1}{\mathcal{P}'}\right)\right]$ and amplification factor G obtained for various types, duration and strength of the force pulse.

Figure S2 shows the values of angle $\Phi = \frac{1}{2}\,\mathrm{atan}\,\Psi$ and amplification G for various force pulse type, duration and strength. The values of angle Φ in Fig. S2a-c show how the duration of both rotation phases $\bar{\tau}_1$ and $\bar{\tau}_3$ differ from the value of $\pm\pi/4$. In the case of the free-motion pulse, we see a gradual increase from 0 to $\pi/4$ as the pulse duration increases. In the case of the harmonic force pulse (parabolic potential) we select one of the complementary solutions $(\bar{\tau}_1,\, \bar{\tau}_3,\, G)$ and $(\bar{\tau}_1',\, \bar{\tau}_3',\, G')$ that give higher amplification G. Figure S2**b** shows the angle Φ changes between $-\pi/4$ and $\pi/4$ with abrupt jumps caused by a selection of a different solution. In the case of an inverted harmonic force (inverted parabolic potential) pulse the angle smoothly decreases from free-fall values for $\Omega_i/\Omega_c = 0$ towards 0 which appears for $\Omega_i/\Omega_c = 1$ independently on the inverted force pulse duration $\bar{\tau}_2$. Further, the values of Φ become negative. It is also noteworthy, that for the inverted force pulse having strength $\Omega_i/\Omega_c > 0.5$ and the pulse duration $\bar{\tau}_2 > \pi/2$ the angle Φ becomes independent on the pulse duration.

Figure S2d-f consequently shows the calculated values of the amplification gain G. In the case of the free motion pulse the gain grows linearly with pulse duration $\bar{\tau}_2$ that are $\gtrsim \pi$. The harmonic force pulse leads to a complex behavior of the amplification gain. However, the gain in this force pulse type is always smaller than in the case of free motion as the translation and expansion of the state during the pulse is slowed down by the harmonic restoring force. $G \equiv 1$ appears when $\bar{\tau}_2 = n\pi\Omega_c/\Omega_p$ (n is an integer number) which corresponds to hyperbolic-like regions in Fig. S2**e**. Lastly, the amplification gain obtained by the inverted linear force pulse is depicted in Fig. S2f. In this case, the gain increases exponentially with both pulse strength (Ω_i/Ω_c) as well as with its duration. Please note the logarithmic scale of the color map. For the plotted parameters, the gain may reach over 10^{10} for the pulse duration $\bar{\tau}_2 = 4\pi$ and the pulse strength $\Omega_i/\Omega_c = 2$. However, gain $G \sim 100$ can be achieved by a weak pulse of strength 0.5 and pulse duration of 2π. This pulse duration corresponds to just a single period of the particle motion in the harmonic potential prior the inverted harmonic force pulse. Moreover, Fig. S3 directly compares the amplification G obtained for IPP, WPP, as well as free motion pulses of various strengths (different Ω_p or Ω_i) and lengths $\bar{\tau}_2$. Here, we can directly see periodic behavior of G induced by WPP, identically unit gain for $\Omega_p = \Omega_c$ (i.e. no change in force) as well as exponential growth of G for IPP.

The Eqs. (S156–S158) also show a possibility of amplifying position ($|G| > 1$) or velocity ($|G| < 1$) with amplifier corresponding to classical non-inverting ($G > 0$) or inverting ($G < 0$) one by a proper selection of the times $\bar{\tau}_1$ and $\bar{\tau}_3$. This is demonstrated in Fig. S4 of all 3 types of force pulses (free motion, WPP, and IPP) with each row corresponding to one of these force pulse types. Left hand side column shows the possible values of G as a function

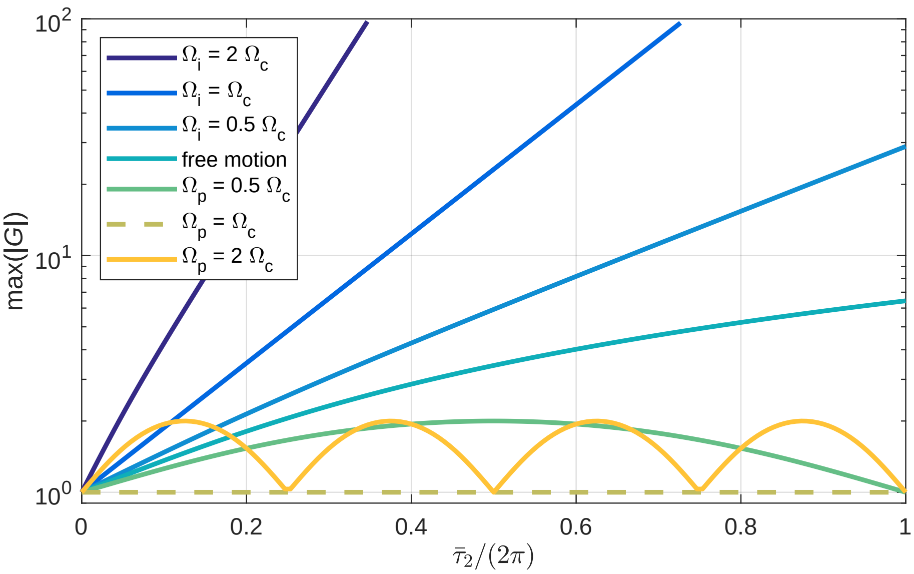

Fig. S3 | Comparison of maximal gain G for various types and strengths of force pulses as a function of force pulse duration $\bar{\tau}_2$.

of the force pulse length $\bar{\tau}_2$. Various line styles combined with symbols depict the 4 modes of amplifier function (position/velocity, non-inverting/inverting). For IPP and WPP each color encodes different strength of the force pulse (frequencies Ω_p,Ω_c. We see, that amplification G in the case of free motion and IPP is unbounded (with much faster growth in IPP case). On the other hand a maximal boundary on G exist in the WPP case that cannot be overcome by bigger $\bar{\tau}_2$. The times $\bar{\tau}_1$ and $\bar{\tau}_3$ leading to these gains are plotted in columns 2 and 3 of Fig. S4. The color, line style, and symbol encoding corresponds to the first column. We can see that while some solutions identically overlap they can be distinguished by the used symbols. Interestingly for FM and IPP, position gain (both inverting/non-inverting) is given by the same time $\bar{\tau}_1$ and inverting/non-inverting type is selected by $\bar{\tau}_3$. In the case of velocity gain the selection of G sign is done by $\bar{\tau}_1$ and $\bar{\tau}_3$ is the same for both inverting and non-inverting cases. In the case of WPP, the relation of amplifier types and both time intervals $(\bar{\tau}_1, \bar{\tau}_3)$ become complex due to periodic behavior and various jumps between solutions. It is also noteworthy, that if one aims to minimize the photon recoil (interaction of a particle with light) in the quantum regime by aiming for minimal sum of $\bar{\tau}_1 + \bar{\tau}_3$ the amplifier function will be an inverting one ($G < 0$) with position/velocity amplification selected by order of $\bar{\tau}_1$ and $\bar{\tau}_3$.

Let us further perform and outlook towards the amplification of a *quantum* state that is close to the quantum ground state using the classical description. The full quantum description will be given in the following Section S1.8. In this case we will perform a normalization with respect to the ground state zero instead of previously used initial state. Figure S5a,b shows the evolution of the state having initial mean values (-1, 0.5) in the form of multiple circles/ellipses having color that corresponds to time. Each ellipse is centered around the mean value in given time while its semi-axes and ordination determine the time dependent covariance matrix. Figure S5a demonstrates the amplification protocol performed at low pressure 10^{-9} mbar and higher pressure 1.6×10^{-6} mbar. In the case of higher pressure we clearly see the reheating effects demonstrating as an increase of ellipse area. The result of the protocol (in both cases) is the amplification of position coordinate with gain $G = 2$, see Figs. S5c,e which depict the evolution of the mean values. Similarly, the evolution of the major and minor ellipses semi-axes is plotted in Figs. S5d,f. At low pressure, the change of semi-axes appears only during expansion/squeezing phase, while for the higher pressure the reheating influences the whole amplification process. However, we see that for both pressures the minor semi-axis $\sigma_{\min}$ becomes squeezed bellow value of 1, i.e. it shows the possibility of quantum squeezing bellow ground state. However, at higher pressure this is possible only in a limited time window. This result would be properly described by means of quantum theory in Section S1.8.

S1.7.1 Additional constant force during force pulse

If there is a non-zero offset $\bar{\Delta}_c$, see Eq. (S128), the phase space coordinates of the amplified state $\mathbf{x}_F$ can be expressed in an analogy with Eq. (S148) as

$$\mathbf{x}_f \quad = \quad \mathbf{R_3}\left[\mathbf{P}\left(\mathbf{R_1}\mathbf{x_0} + \bar{\boldsymbol{\Delta}}_c\right) - \bar{\boldsymbol{\Delta}}_c\right]$$

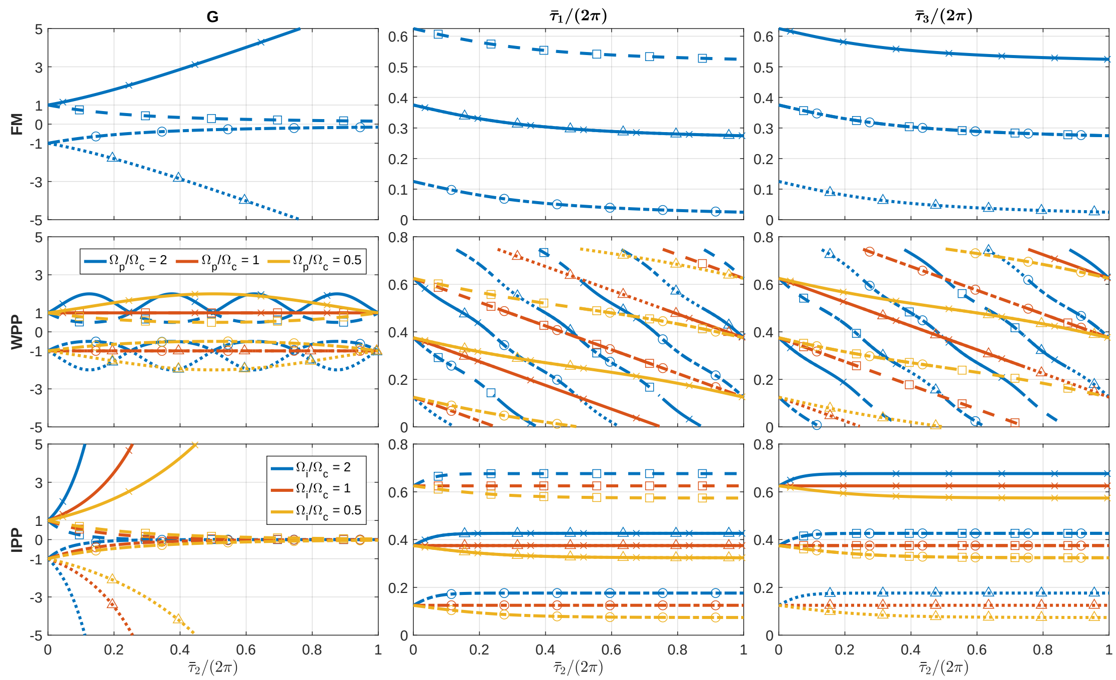

Fig. S4 | Demonstration of positive and negative gain amplification or squeezing and corresponding times $\bar{\tau}_1$ and $\bar{\tau}_3$ for various force pulse types and strengths. rows, Each row correspond to different force pulse type, i.e. free motion (FM), weak parabolic potential (WPP) or inverted potential (IPP). **Column 1**, Gain calculated using Eq. (S158). Solid curve marked by squares correspond to positive position amplification ($G > 1$), dashed curve marked by triangles correspond to positive position squeezing ($0 < G < 1$), circles marked dotted curves corresponds to negative amplification ($G < -1$) and $\times$ marked dash-dot curve corresponds to negative squeezing ($-1 < G < 0$). Colors of the curves in rows 2 and 3 correspond to different force pulse strengths characterized by frequencies Ω_p or Ω_i. **Columns 2-3**. Times $\bar{\tau}_2$ and $\bar{\tau}_3$ calculated using Eqs. (S156, S157) that give amplification factor G depicted in **column 1**. Line style, symbol, and color coding correspond to **column 1**. When 2 solutions identically overlap, the curves may be distinguished by 2 types of symbols on each curve.

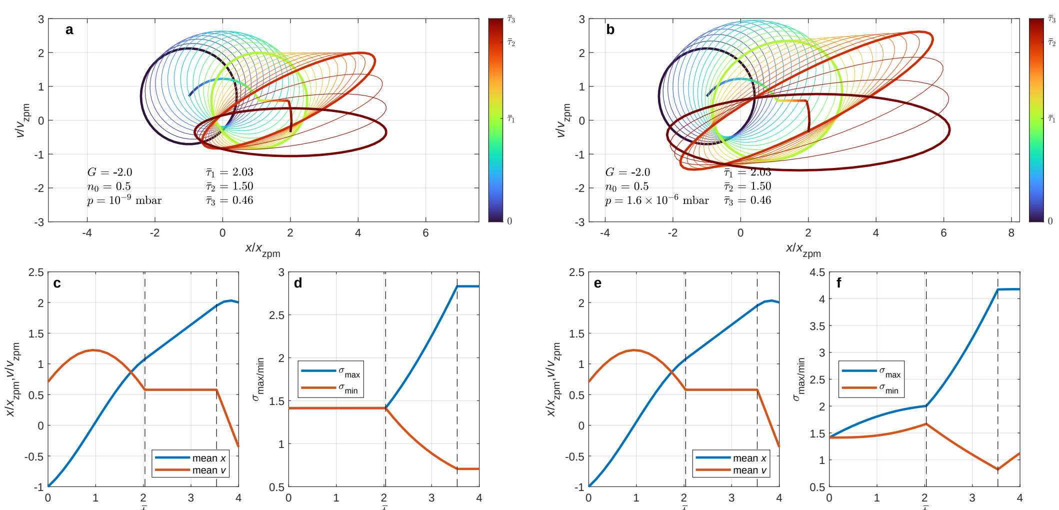

Fig. S5 | State evolution using the full analytical classical equations from the quantum like initial state corresponding to occupation number $n_0 = 0.5$. a-b, State evolution for 2 different damping rates (ambient pressures) at different times depicted by an ellipse of different colors. The positions and velocities are normalized to the zero-point fluctuations. Strong reheating is visible for the larger pressure 1.6×10^{-6} mbar (**b**) considered in following Section S1.8. The thick ellipse boundaries indicates the beginning and the end of each of the three steps and the evolution of the mean values (corresponding to the ellipse centers) is depicted by colored curve. The time is color-coded. **c,e**, Evolution of the mean position (blue) and velocity (red). **d,f**, Evolution of the major $\sigma_{\max}$ (blue) and minor $\sigma_{\min}$ (red) semiaxis of the state. $\sigma_{\min} < 1$ demonstrates possibility of squeezing below quantum ground state. Vertical dashed lines in **c-f** show times $\bar{\tau}_1$ and $\bar{\tau}_2$.

$$= \quad \mathbf{R_3PR_1x_0} + \mathbf{R_3} \begin{pmatrix} \mathcal{A}-1 \\ \frac{1}{\mathcal{P}'}\mathcal{B} \end{pmatrix} \bar{\Delta}_c, \tag{S162}$$

$$\bar{\mathbf{\Delta}}_c \quad = \quad \begin{pmatrix} \bar{\Delta}_c \\ 0 \end{pmatrix}. \tag{S163}$$

In principle, Eq. (S162) shows that the initial phase spaces position would be transformed in the same way as in the case without additional constant force. However, independently of the initial position, an extra, constant, phase space shift will appear, that depends on the additional force, the pulse, and the rotation in the third phase. Therefore, the initial phase space position transformation could be selected according to the Bloch-Messiah transform. The final phase space position would be the combination of the amplified initial position given by Eqs. (S154, and S155) that are phase space shifted by an offset in both position and velocity as follows

$$x_F \quad = \quad Gx_0 + \bar{\Delta}_c \left[\quad (\mathcal{A}-1)\cos\bar{\tau}_3 + \frac{1}{\mathcal{P}'}\mathcal{B}\sin\bar{\tau}_3 \right], \tag{S164}$$

$$v_F \quad = \quad \frac{1}{G}v_0 + \bar{\Delta}_c \left[-(\mathcal{A}-1)\sin\bar{\tau}_3 + \frac{1}{\mathcal{P}'}\mathcal{B}\cos\bar{\tau}_3 \right]. \tag{S165}$$

S1.8 Quantum squeezing of motion

As the residual gas is evacuated from the vacuum chamber and its pressure decreases, the role of collisions with the gas molecules in the heating of the nanoparticle (NP) becomes negligible. The dominant source of dissipation in the high-vacuum regime becomes the random elastic scattering of the photons of the trapping light to stray light modes. This effect is termed in the literature as *recoil heating*[?, ?]. In this section, we investigate the attainable quantum squeezing given a sufficiently low initial temperature of the mechanical oscillator and a high vacuum so that the recoil heating becomes the dominant heating source.

To study the attainable quantum squeezing, we will need to compare eigenvalues of the covariance matrix of the NP's canonical position and momentum quadratures with the ground state variance. This is most conveniently done using the dimensionless canonical quadratures (q, p) such that $[q, p] = 2\mathrm{i}$, so that the ground state variance equals one. Starting with the dimensional canonical quadratures x and P, we can rewrite the Hamiltonian

$$H = \frac{P^2}{2m} + \frac{1}{2}m\left[\Omega_t(t)\right]^2 x^2 = \frac{\hbar\Omega_c}{4}\Big[p^2 + \xi(t)q^2\Big], \tag{S166}$$

where $\Omega_t(t)$ is the instantaneous value of the trapping frequency, Ω_c (used in the main text) is the base value of this frequency, $\xi(t) = (\Omega_t(t)/\Omega_c)^2$ is the frequency reduction coefficient that embodies the capabilities of the experimental setup to change the trapping stiffness. The dimensionless quadratures are defined as

$$q = x\sqrt{\frac{2m\Omega_c}{\hbar}}, \quad p = P\sqrt{\frac{2}{\hbar m\Omega_c}}. \tag{S167}$$

Note that the base value of the frequency Ω_c enters the definition of q and p. Consequently, quantum states showing no squeezing at one value of the base frequency Ω_c can appear squeezed at a different base frequency $\Omega_c' \neq \Omega_c$. We shall note in passing that trapping the NP in an inverted quadratic potential formally corresponds to a negative value of Ω_t^2 in (S166) and consequently a negative value of ξ.

Dynamics of the NP is governed by the Langevin-Heisenberg equations. The recoil heating manifests itself as an additional stochastic force acting on the NP. Consequently, the Langevin equations of motion (S5) can be generalized as:

$$\dot{q}(t) = \Omega_c p(t), \tag{S168a}$$

$$\dot{p}(t) = -\Omega_c\xi(t)q(t) - (\Gamma_{\mathsf{rec}} + \Gamma_{\mathsf{gas}})p(t) + \sqrt{2\Gamma_{\mathsf{rec}}}\eta_{\mathsf{rec}}(t) + \sqrt{2\Gamma_{\mathsf{gas}}}\eta_{\mathsf{gas}}(t). \tag{S168b}$$

Here, $\Gamma = \Gamma_{\mathsf{rec}} + \Gamma_{\mathsf{gas}}$ is the mechanical damping rate with contributions Γ_{gas} from the collisions with the residual gas molecules and Γ_{rec} from the recoil heating. Correspondingly, $\eta_{\mathsf{gas}}(t)$ is the noise force associated with the gas damping, and $\eta_{\mathsf{rec}}(t)$ is the stochastic force associated with the recoil heating. Both noises obey standard Markovian correlation relation $\frac{1}{2}\langle\eta_i(t)\eta_i(t') + \eta_i(t')\eta_i(t)\rangle = (2n_i + 1)\delta(t - t')$ with variance proportional to the effective thermal occupation n_i of the corresponding noise source. The noises can be effectively quantified by the so-called *heating rates* $H_i = \Gamma_i(n_i + 1/2) \approx \Gamma_i n_i$. These quantities show the rates at which individual phonons from the environment get admixed to the NP's motion

The recoil heating rate can be estimated as[?]

$$H_{\text{rec}} = \frac{1}{5}\frac{P_{\text{scatt}}}{mc^2}\frac{\omega_0}{\Omega_t}, \tag{S169}$$

where m is the NP mass, ω_0 is the light frequency. The power P_{scatt} scattered by the particle is given by the product of the scattering cross-section σ_{scatt} and the intensity I_0 at the NP's location:

$$P_{\text{scatt}} = \sigma_{\text{scatt}} \times I_0 = \frac{1}{6\pi\epsilon_0^2}\left|4\pi\epsilon_0 R^3 \frac{n^2-1}{n^2+2}\right|^2 k^4 \times P_0 k^2 (\text{NA})^2/2\pi = \frac{256}{3}P_0(\text{NA})^2\left(\frac{\pi R}{\lambda}\right)^6\left|\frac{n^2-1}{n^2+2}\right|, \tag{S170}$$

with R being the NP's radius, ϵ_0 vacuum permittivity, n refraction index, $k = 2\pi/\lambda$ the wavevector of the trapping light, λ the wavelength of the trapping light. Importantly, the heating rate depends on the particle's trapping configuration, in particular, trapping power P_0 and numerical aperture (NA). In the setup considered here, the base value of the recoil heating rate attained at the strongest trapping power can be estimated to be of the order $H_{\text{rec},0} \approx 1.4 \times 10^5$ Hz.

The heating by the collisions with the residual gas molecules is characterized by the rate[?] :

$$H_{\text{gas}} \approx 15.8\frac{R^2 p_{\text{gas}}}{m\sqrt{3k_{\text{B}}T/m_{\text{gas}}}}\frac{k_{\text{B}}T}{\hbar\Omega_c}, \tag{S171}$$

where p_{gas} is the gas pressure, m_{gas} is the mass of gas particles, k_{B} is the Boltzmann constant. At room temperature ($T = 300$ K) at approximately $p_{\text{gas}} \approx 1.4 \times 10^{-6}$ mbar, $H_{\text{gas}} \approx H_{\text{rec},0}$.

As the trapping power P gets reduced, both the actual trapping frequency $\Omega_t(t)$ and the recoil heating rate $H_{\text{rec}}(t)$ decrease. The trapping frequency $\Omega_t^2 \propto P$, and hence $|\xi(t)| = P/P_0$. The heating rate $H_{\text{rec}} \propto \sqrt{P/P_0}$ and consequently $H_{\text{rec}}(P(t))/H_{\text{rec}}(P_0) = \sqrt{\xi(t)}$.

As we are interested in the squeezing that can be estimated from the covariance matrix of the Gaussian quantum state, it is sufficient for us to limit ourselves to the Lyapunov equation for the covariance matrix $\mathbf{\Theta}$. In contrast with the classical treatment, for the quantum treatment, we use *symmetrized* means of canonical quadratures

$$\mathbf{\Theta} = \begin{pmatrix} \langle q^2 \rangle & \frac{1}{2}\langle qp + pq \rangle \\ \frac{1}{2}\langle qp + pq \rangle & \langle p^2 \rangle \end{pmatrix}. \tag{S172}$$

For simplicity, we consider the initial mechanical state to have zero mean displacement ($\langle q \rangle = \langle p \rangle = 0$), and therefore *all* the quantum dynamics is contained in the dynamics of the covariance matrix. The equivalent Lyapunov equation of Eqs. (S168) reads[?]

$$\frac{\mathrm{d}}{\mathrm{d}t}\mathbf{\Theta} = \mathbf{M\Theta} + \mathbf{\Theta M}^{\mathsf{T}} + \mathbf{D}. \tag{S173}$$

Here $\mathbf{M}$ is the drift matrix whose elements can be extracted from the equations of motion, and $\mathbf{D}$ is the diffusion matrix with the elements capturing covariance of the noise:

$$\mathbf{M} = \begin{pmatrix} 0 & \Omega_c \\ -\xi(t)\Omega_c & -\Gamma \end{pmatrix}, \qquad \mathbf{D} = \text{diag}(0, 4[H_{\text{rec}}(t) + H_{\text{gas}}]). \tag{S174}$$

In the regime considered here, matrices $\mathbf{M}$ and $\mathbf{D}$ are time-dependent via the time dependence of the trapping frequency Ω_t and the heating rate H_{rec}. We model the oscillator's frequency reduction coefficient $\xi(t)$ as a piecewise-linear function of time that changes between $\xi(t \le t_1) = 1$ and a different value $\xi(t') = -|\xi'|$. Switching takes place during the intervals $t_1 \le t \le t_1 + \tau_{\text{r}}$ and $t_2 - \tau_{\text{r}} \le t \le t_2$. Hence this parameter takes values

$$\xi(t \le t_1) = 1; \quad \xi(t_1 + \tau_{\text{r}}) = \xi(t_2 - \tau_{\text{r}}) = \xi'; \quad \xi(t \ge t_2) = 1, \tag{S175}$$

and intermediate values according to a linear law in the intermediate times. Correspondingly, the recoil heating rate changes from the value at the strongest trapping power $H_{\text{rec},0}$ to a reduced value $\sqrt{|\xi'|} \times H_{\text{rec},0}$. Here τ_{r} denotes the duration of the switching interval (during which the frequency (heating rate) changes linearly in time), and τ_{f} denotes the duration of the dynamics in the inverted potential. In the simulations here, $\Omega_c\tau_{\text{r}} = 7 \times 10^{-3}$, and the dynamics of the covariance matrix is barely distinguishable from the analytical solution that can be obtained by appropriate modification of the results of Sec. S1.3.4.

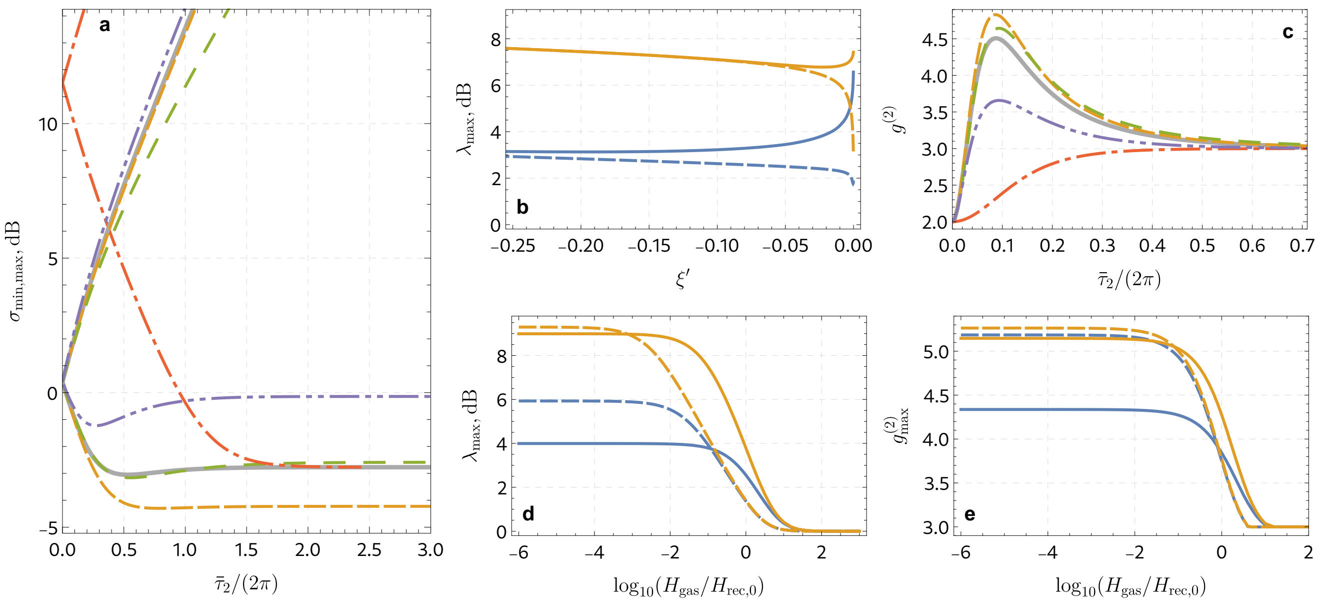

Fig. S6 | Quantum squeezing of motion of the levitated NP. a smallest and largest semiaxes of the noise ellipse (in dB) as a function of time for different parameters. Negative values correspond to squeezing below the ground state variance. In the base set (solid gray lines), $H_{\mathsf{rec},0} = 1.4 \times 10^5$ Hz, estimated for the current experimental setup, $n_0 = 0.5$, $H_{\mathsf{gas}} = 0.01 H_{\mathsf{rec},0}$, attainable at the pressure $p_{\mathsf{gas}} \approx 10^{-8}$ mbar, $\xi' = (\Omega_{\mathsf{IPP}}/\Omega_c)^2 \equiv \xi_0 \approx -0.17$. Other lines correspond to one of the parameters changed. Yellow (densely dashed): recoil heating reduced twofold; green (loosely dashed): $\xi' = \xi_0/2$; red (dot-dashed) initial occupation increased to $n_0 = 100$; purple (double-dot-dashed) gas heating $H_{\mathsf{gas}} = H_{\mathsf{rec},0}$ (corresponding to $p_{\mathsf{gas}} \approx 10^{-6}$ mbar). **b** maximal (solid lines) and steady (dashed lines) values of squeezing attainable as a function of frequency inversion ξ' for two different values of base recoil heating rate $H_{\mathsf{rec},0}$ and $0.1 H_{\mathsf{rec},0}$ assuming gas heating rate $H_{\mathsf{gas}} = 0.01 H_{\mathsf{rec},0}$. **c** intensity autocorrelation $g^{(2)}$ of the NP state as a function of time. Color coding same as in panel (a). **d** maximal squeezing attainable as a function of the gas heating rate H_{gas} in units of the base recoil heating $H_{\mathsf{rec},0}$. Different colors correspond to different value of the recoil heating rate used in simulations: $H_{\mathsf{rec},0}$ for blue and $0.1 \times H_{\mathsf{rec},0}$ for yellow. Solid lines correspond to fully inverted quadratic potential with $\xi' = -1$, dashed lines nearly to the regime of the free fall $\xi' = -10^{-3}$. **e** maximal value of $g^{(2)}$ as a function of the gas heating. Color coding same as in (d). In (d,e), $n_0 = 0.1$.

Assuming the initial state of the NP at $t = t_1$ to be thermal with mean occupation n_0, the initial covariance matrix reads $\mathbf{\Theta}(0) = (2n_0 + 1)\mathbf{1}_2$, where $\mathbf{1}_2$ is a 2×2 identity matrix. The initial mean occupation is related to the effective temperature T_0 via Bose-Einstein distribution: $n_0 = \left[\exp[\hbar\Omega_c/k_{\mathsf{B}}T_0] - 1\right]^{-1}$. Having the initial covariance matrix $\mathbf{\Theta}(0)$ and explicit time dependence of the drift and diffusion matrices $\mathbf{M}, \mathbf{D}$, one can solve the Lyapunov equation for the covariance matrix $\mathbf{\Theta}(t)$ as a function of time numerically. Results of our simulations are in Fig. S6, where we investigate the squeezing of the mechanical state as a function of the experimental setting. The squeezing is estimated from the covariance matrix as

$$\lambda(t)[\mathrm{dB}] = \max\left[0, -10\log_{10}(\sigma_{\mathsf{min}}(t))\right], \tag{S176}$$

where $(\sigma_{\mathsf{min}})^2(t)$ is the smallest eigenvalue of $\mathbf{\Theta}$.

We perform our simulations using numerical parameters corresponding to the current setup (base value of the recoil heating $H_{\mathsf{rec},0}$) and investigate hypothetical scenarios of recoil heating decreased (e.g. by using smaller particles). Initial occupation values are chosen in the region $n_0 \leq 1$, reachable with the state of the art technology[?] .

From our studies, it follows that in each experimental run, motion in the altered potential creates correlations between the quadratures that manifest in quantum squeezing. The time it takes σ_{min} to reach squeezed state is determined by the initial spread of the thermal state in the phase space, set by the initial occupation n_0. The rate at which the squeezing increases initially, is defined by the values of the stiffness of the inverted potential ξ' and the heating rates. During the initial time interval, the squeezing grows until a certain point where the heating prevents subsequent squeezing. This can be explained geometrically. Correlations between the quadratures generate squeezing that manifests itself as a reduction in the minor semiaxis associated with the covariance matrix of the NP's quantum state. The noise contributes mostly in enlargement of the ellipse in the direction of the p quadrature of the NP, which happens to be misaligned with the direction of the squeezing axis. This allows reaching maximal value of squeezing after shorter durations of the evolution (Fig. S6b, solid lines).

Eventually, the squeezing reaches the steady value. The NP itself does not have a motional steady state which is intuitively clear as the NP is in a potential without local minima, and can be proven formally as all eigenvalues of $\mathbf{M}$ have positive real parts (existence of a stable steady state requires the eigenvalues to have negative real parts). The steady value of squeezing is determined by the interplay of the frequency inversion and the heating rates. As shown in Fig. S6a the steady value of squeezing obviously increases with decrease of the base value of the recoil heating, and increases with the increase of the stiffness of the inverted potential.

As it follows from Fig. S6b, in the case of vanishingly small gas damping, the optimal strategy is the free fall of the NP when, in absence of light, there is no recoil heating. Consequently, the evolution is nearly unitary and in theory can reach arbitrary values. In practice, there is always a source of heating, moreover, squeezing increases the spread of the NP state in the phase space, so that eventually it reaches the region of nonlinear tweezer potential, or ultimately escapes the tweezer altogether. The maximally attainable squeezing as a function of gas heating rate is shown in Fig. S6d.

To evaluate the potential non-classical properties of the squeezed state, we evaluate the second-order (intensity) autocorrelation of the mechanical motion at zero delay (Fig. S6c). We define this function as

$$g^{(2)}(t) = \frac{\left\langle \left(a^\dagger(t)\right)^2 \left(a(t)\right)^2 \right\rangle}{\left\langle a^\dagger(t) a(t)\right\rangle^2}, \tag{S177}$$

where $a = (q + \mathrm{i}p)/2$, $[a^\dagger]$ is the annihilation [creation] operator of the NP's motion. Squeezing of a thermal state with sizeable occupation monotonously changes its intensity autocorrelation from 2 to 3, in accordance with basic theory. In this regime, $g^{(2)}(t)$ never exceeds 3. Simultaneously, starting with a state of higher purity (equivalently, of lower occupation, e.g. $n_0 = 0.1$, as in Fig. S6a), we observe the values of $g^{(2)}(t) > 3$ at intermediate times. At later times, where there is a sufficient contribution of noise, and the squeezing approaches its steady value, the intensity autocorrelation function saturates to $g^{(2)}(t) = 3$. Thus, $g^{(2)}(t) > 3$ serves an indicator of sufficiently pure quantum squeezing. In Fig. S6e we evaluate the maximal attainable values of $g^{(2)}$ as a function of the residual gas heating rate. Our simulations indicate that at the current value of the recoil heating rate and comparable gas heating (i.e., pressures $p_{\mathsf{gas}} \approx 10^{-6}$ mbar), it is possible to obtain $g^{(2)} > 3$. Further simulations show that at these heating rates, the requirement for this is $n_0 \lesssim 1$, compatible with present technology[?] .

S2 Experimental details

S2.1 Experimental setup

The detailed experimental setup is drawn and commented in Fig. S7. Below we provide a fast list of the key hardware we used:

1. Laser: wavelength 1064 nm, output power 3 W, type Mephisto, Coherent
2. AOM A: Gooch & Housego Fiber-Q - 1060 nm Fiber Coupled Acousto-Optic Modulator, frequency upshifted by 150 MHz
3. AOM B: Gooch & Housego Fiber-Q - 1060 nm Fiber Coupled Acousto-Optic Modulator, frequency downshifted by 150 MHz
4. GENER: High-frequency generator: Keysight N5171B
5. DRIVER: Gooch&Housego 2.5 W RF driver
6. PICO: Picoscope 6000E used for fast data acquisition.
7. FPGA: National Instruments card 5783
8. QPD: Homemade quandrant photodetector
9. BD: PDB415C-AC (Thorlabs)
10. particles of radius ≈ 150 nm (Bangs Laboratories)

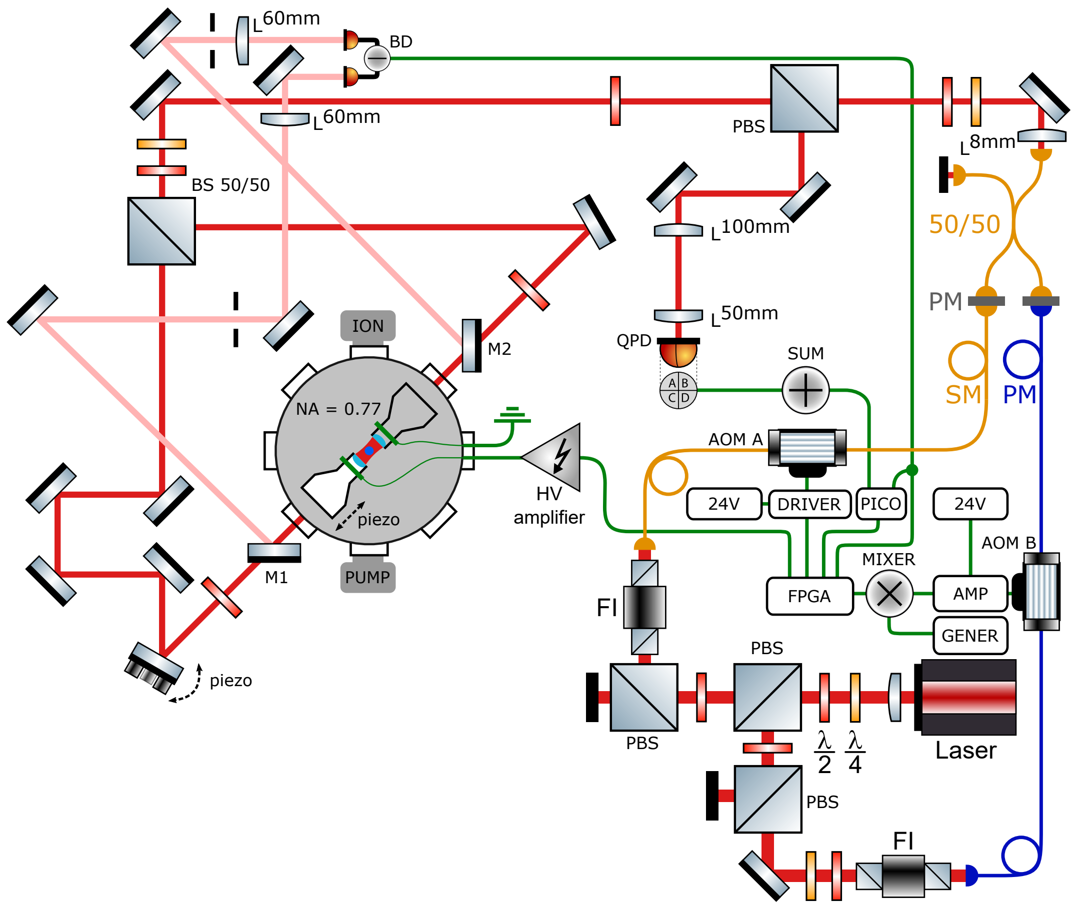

Fig. S7 | Experimental setup. The beam from the laser is split at the first polarizing beam splitter (PBS). A pair of the second PBSs and halfwave plates control the power distribution in the system. The yellow (single mode optical fiber SM) and blue (polarization maintaining optical fiber PM) form the parabolic and inverted parabolic potential, respectively. There is one Faraday isolator (FI) and one AOM in each path. Yellow and blue paths are coupled by 2x2 fiber coupler into one beam, collimated by $L^{8\,\mathrm{mm}}$, and polarization controlled and split at the non-polarizing 50/50 beam-splitter. The whole setup forms a Michelson-Sagnac interferometer with different lengths of optical paths. Both counter-propagating beams enter the vacuum chamber where they are focused (NA=0.77) and form a standing wave along the beam propagation. An external electric field of the cold damping feedback is applied via the HV amplifier to the lens holders (green wires). The detection of the axial particle position is done through 10% reflective mirrors (M1, M2) and balanced detector BD. The lateral particle motion is detected by the quadrant photodetector QPD. The signals of particle positions are recorded by the Picoscope (PICO).

S2.2 Detection

The position detection of the trapped particle is based on homodyne detection where the trapping beam acts as a local oscillator. The principle of the detection is depicted in Fig. 5 of the main text. The scattered light is modulated in phase due to particle movement and interferes with the trapping beam. Since we have two counter-propagating trapping beams, we can collect information about particle motion from both sides and in a regime of balanced detection, the intensity offset is subtracted and the full dynamic range of the detector and acquisition device is used. This dramatically improves the signal-to-noise ratio because suppresses classical noise in the laser light and cross-talks with other axes (see Fig. S8). The reflected detection beams are focused on the photodiodes and dimmed just below the saturation level of the detector. The signal-to-noise ratio is optimized by setting the proper diameter of the iris apertures and the distance of the lenses from the detector.

S2.3 Measurement procedure

The measurement procedure is described in Methods of the main text. Figure S9 shows the measured raw data obtained during the reference (even repetitions) and force pulse (odd repetitions) during Step II. The balanced detector signal in Fig. S9a corresponds to the particle trapped during the reference measurement. The particle

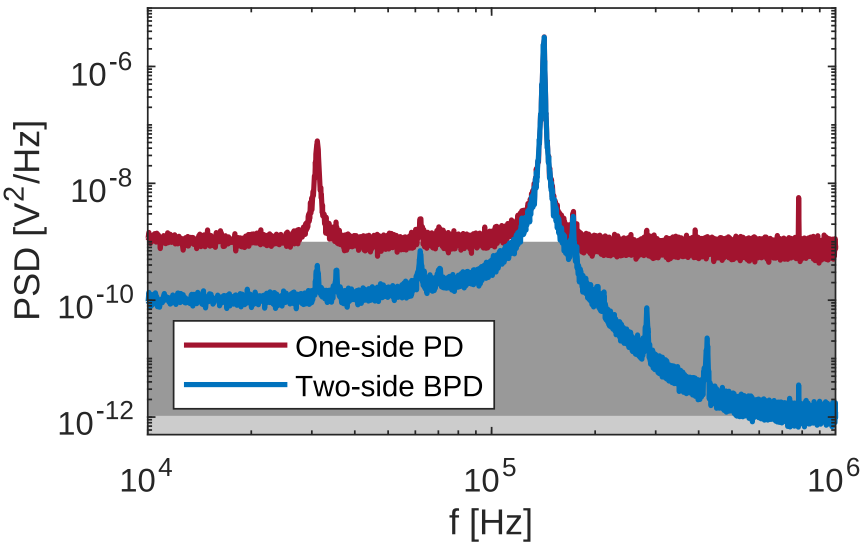

Fig. S8 | Comparison of z-position signals detected by a single DC coupled photodiode placed just in one arm (red) and balanced detector using two arms (blue).

oscillations are lower during active cold damping at $t < 0$ μs and $t > 42$ μs. On the contrary, the balanced detector signal plotted in S9b is obtained during an inverted potential pulse of duration $\tau_2 = 2$ μs. One can easily see the spikes in signal due to the transient effects in the detection electronics which give a "virtual signal" not directly related to the particle motion. The signal is recovered after $t \simeq 3$ μs and the particle oscillates with larger amplitude. Figures S9c and d monitor the power of the harmonic trap, i.e. the laser beam that is not shifted in a frequency. During the reference measurement, the total power (and thus the optical tarp strength) is not changed. However, when the inverted force pulse is applied (see Fig. S9d) we observe the attenuation of the incident power to ~ 17 % of the original value. In order to discriminate between all phases of the experimental protocol we also record the control signal generated internally by the FPGA card, see Fig. S9e and f. Each voltage level exactly identifies the phase of stroboscopic protocol and links it to the positional signals.

S2.4 Data processing

The multiple trajectory records are firstly sorted into reference and pulse groups based on the value of the control voltage; for each trajectory in both groups the exact start of the potential switch is located in the control signal and all trajectory records are aligned to this point, i.e. time $t = t_1$ (considering Fig. 1 of the main text). Further, the data are low-pass filtered by the Sawitsky-Golay filter of the third order and width of 15 points, and the mean value during the active cold damping at $t < 0$ is subtracted. Then the particle velocity is calculated as the second-order central difference of the positions.

The data corresponding to Steps II, III, and reading step contain a period of dead time when the detected signal is strongly influenced by electronic transition effects. The dead time was determined to be ≈ 3 μs from the decrease of the ensemble mean signal to zero after a free-motion period of various durations.

S2.5 Transformation to normalized coordinates

As we mentioned in the main text, we use normal coordinates where the normalization factor is the standard deviation of the particle position or velocity in the thermal equilibrium state in the parabolic potential. Only trajectories taken during the reference (even) repetition of the protocol are used to avoid unwanted correlations between the normalization factors and the evaluation of the particle behaviour due to the potential switch. Finally, the ratio of standard deviations of velocity and position gives us a method to determine the oscillation frequency.

It turns out that this way is sufficiently precise for our experimental conditions. As the trajectory record is composed of thousands of short-time trajectory snippets the standard procedure of calculation of power spectral density is not appropriate. For another determination of the oscillation frequency, we used the evolution of the experimental trajectory in the phase space. As the ideal harmonic oscillator is described by a rotation matrix we determined an angle ϕ between a trajectory starting phase space position at a reference time $\bar{t}_r$ and phase space

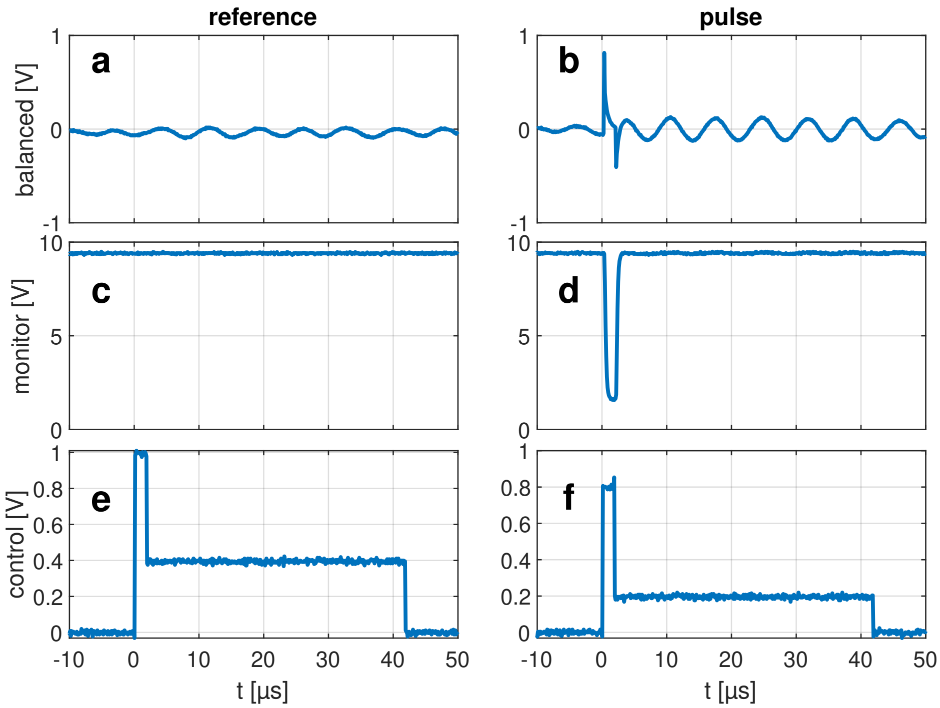

Fig. S9 | Measured raw signals. **a**, Signal output of the balanced detector for a particle moving in parabolic potential (i.e. during the reference repetition). **b**, The peaks close to t=0 denote the switch of the potential profiles from parabolic to inverted parabolic. The recovery of the positional signal takes about 5 ns. The following periodic oscillations (of larger amplitude compared to **a**) correspond to the amplified particle motion in parabolic potential during Step III and reading step (see Fig. 1 of the main text). **c**, Power in the optical path corresponding to the parabolic trapping potential during the reference repetitions. **d**, The same power as in and **c** during the potential switch **d** over $0 <= t <= 2\mu$s. **e-f**, Control signal is recorded together with data acquisition and codes the steps of the experimental protocol. It is used as a time stamp during data post-processing. The meaning of the control signal levels: **0 V:** cold damping feedback is active; **0.2 V:** the parabolic potential is on after the potential switch (Step III and reading step after the potential switch) **0.4 V:** the parabolic potential is on during the reference measurement (even repetitions of Step II) **0.8 V:** inverted parabolic or weak parabolic potential is on in Step II. **1 V:** parabolic potential is on (reference measurement) during Step II.

position point in a certain time $\bar{t}$ for every measured trajectory. Assuming negligible damping the angle $\phi(\bar{t})$ is

$$\phi(t) - \phi(\bar{t}_r) = -\frac{\Omega_\phi}{\Omega_c}\left(\bar{t} - \bar{t}_t\right), \tag{S178}$$

where Ω_ϕ/Ω_c is the ratio of frequency obtained by phase space rotation and by the procedure described above using the ratio of standard deviations. Figure S10 shows the histogram of angles ϕ at given time $\bar{t}$ (each column represents an angle histogram in a particular time) for a selected reference time $\bar{t}_r = -10\pi$. The least-square fits of the slope gives $\Omega_\phi/\Omega_c =\sim -1.00138 \pm (2 \times 10^{-5})$, denoted by the red lines in Fig. S10. The difference in the frequencies is just $(\Omega_\phi - \Omega_c)/2\pi = 190$ Hz. This small difference is probably caused by a combination of damping and/or small contributions of non-linear effects.

S2.6 Determination of the shift between the parabolic inverted parabolic potentials

Due to an experimental misalignment, there is some spatial shift between the standing wave anti-node and node forming the parabolic and inverted parabolic potentials, respectively. This misalignment effectively gives rise to the constant force F_c acting on the particle. In normalized coordinates the force may be characterized by an offset $\bar{\Delta}_c$, see Eq. (S128).

Let us assume the initial state prior potential switch is of zero means in both position and velocity, i.e. $\bar{\mu}_x = \bar{\mu}_v = 0$. Due to the presence of the constant force F_c the mean values would be shifted in phase space according to Eqs. (S129, and S130). During the reading step of motion in harmonic restoring force the mean value of the phase space state would follow the circular trajectory (assuming no damping). The mean radius of the phase space motion is

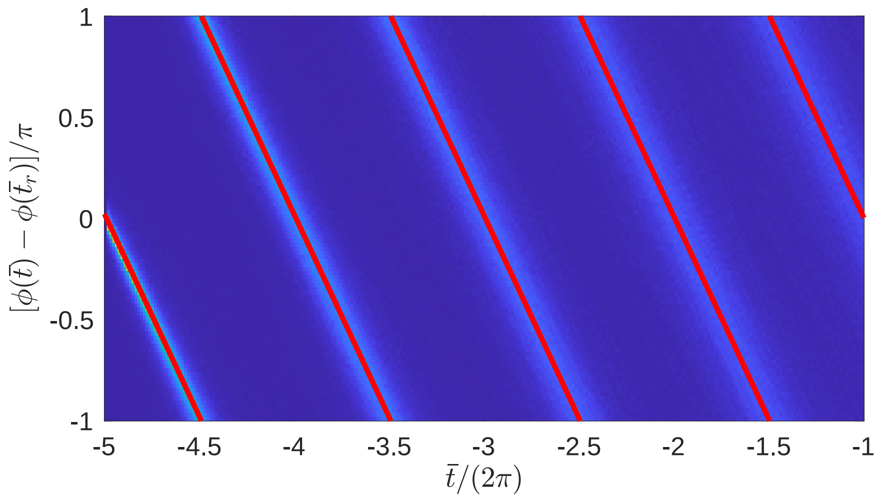

Fig. S10 | Histogram of the angle ϕ which describes the rotation of a phase space position in restored parabolic potential (reading step) taken with respect to the reference angle at time $\bar{t}_r = -10\pi$. Each column corresponds to an individual histogram of angles in a given time and the red lines depict the averaged time evolution if ϕ.

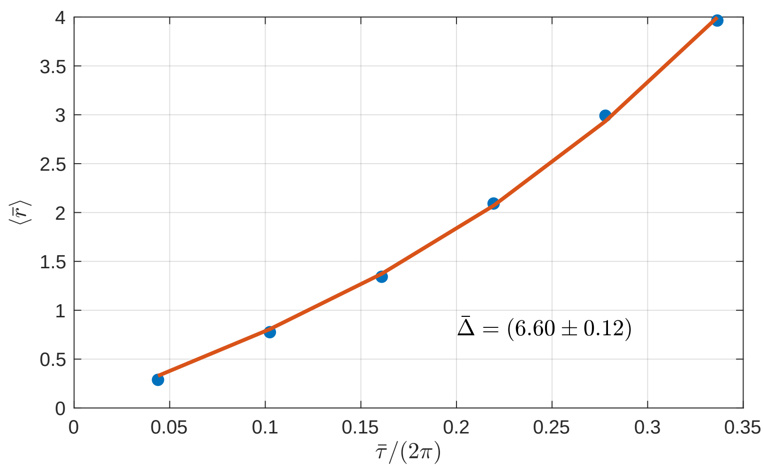

Fig. S11 | Experimental determination of the shift Δ_c between the position the IPP maximum and the minimum of the parabolic potential as described by Eq. (S179).

then

$$\langle \bar{r} \rangle = |\bar{\Delta}_c| \left[\frac{\Omega_i^2}{\Omega_c^2} \sinh^2 \frac{\Omega_i}{\Omega_c} \bar{\tau}_2 + \left(\cosh^2 \frac{\Omega_i}{\Omega_c} \bar{\tau}_2 - 1 \right)^2 \right]^{\frac{1}{2}}, \tag{S179}$$

where $\bar{\tau}_2$ is the duration of the force pulse (squeezing) phase and the ratio of frequencies Ω_i/Ω_c can be determined from the relative change of the laser power. In the experiment, the value of $\langle \bar{r} \rangle$ could be evaluated using a reasonably short time trace of phase space means, i.e. the time scale where the damping is negligible. Using the radii determined from several values of $\bar{\tau}$ one may obtain the value of $|\bar{\Delta}_c|$ while its sign may be determined using the sign of mean velocity after the pulse, see Eq. (S130). Figure S11 shows the experimental result (blue dots) for six values $\bar{\tau}_2$. The red curve gives the Eq. (S179) for fitted value $\bar{\Delta}_c = (6.60 \pm 0.12)$, which corresponds to $\Delta_c \approx 73$ nm. Due to the fact, that the mean velocity after the IPP switch is positive (see the second row and second column in Fig. S13) the value of $\bar{\Delta}_c$ is indeed positive.

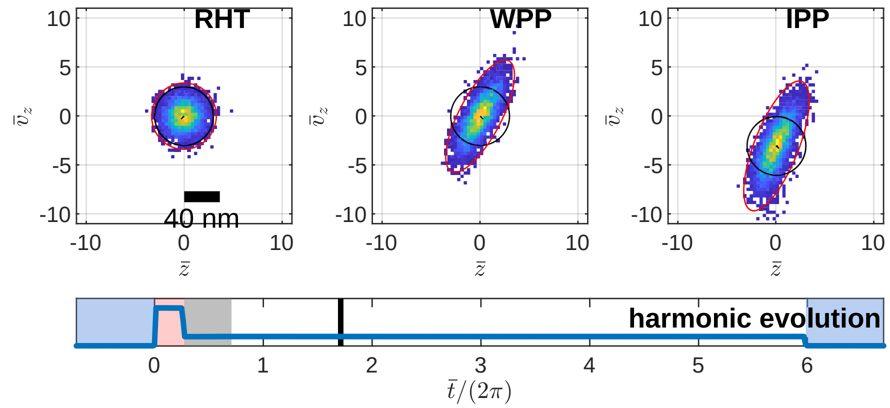

Fig. S12 | Examples of the reconstructed phase space probability distributions (PSPDs) at time $\bar{t} = 2\pi + \bar{\tau}_2$ ($\bar{\tau}_2 = 0.51\pi$) from the reference repetitions (RHT), weak parabolic potential (WPP), and inverted parabolic potential (IPP). The second row illustrates the process. Background blue - cooling, pink - potential switch (Step II), grey - the dead time (recovery of the position signal) (the first part of reading step), white - reading step, blue end - cooling of the next repetition of the sequence. The PSPD time evolution for WPP and IPP can be seen in the Supplementary Movie 1.

S3 Results

S3.1 Evolution of mean values and covariance matrix

Figure S12 shows a comparison of the reconstructed experimental two-dimensional phase space ($x - v$) probability density after for potential switch of duration $\bar{\tau}_2 = 0.51\pi$ in time $\bar{t} = 2\pi + \bar{\tau}_2$. The left panel shows the PDF for the case of the reference measurement (pure reheating RHT during the even repetitions), the middle and right panels depict the PDF obtained during the applied WPP and IPP, respectively. The black circle denotes in the normal coordinates the "unit circle" of radius 3 while the red ellipse shows the same distance in the coordinates based on the eigenvectors of the covariance matrix (Mahalanobis distance). In both cases, the origin of the coordinate system overlaps with the mean values of position and velocity. The bottom panel shows a phase of the system evolution (see Section S2.3) at the given time $\bar{t}$. Furthermore, the attached supplementary Video 1 depicts the evolution of these PDFs for all times shown in the bottom panel. Please note, that the WPP and IPP PDFs extrapolated over the detector (recovery) dead time (red and grey areas) are plotted in desaturated colors in order to stress their uncertainty.

Figure S13 shows the time evolution of the mean phase space position, velocity, and the elements of the covariance matrix obtained using the experimental trajectories. Each column of Fig. S13 corresponds to one of these quantities and the rows compare the behavior during WPP and IPP at high and low pressures. The thin blue curve in the grey region marks an extrapolation of the observed quantity towards over the dead time to $\bar{t} = 0$.

One can see that the mean phase space position (position and velocity) shows some periodic behavior even in the case of WPP. However, the magnitude of these mean oscillations is very low, on the order of noise, and the observed motion is caused by the finite size of the trajectory ensemble. On the other hand, in the case of IPP, one can observe very clear and deterministic oscillations of mean values caused by the additional force offset. The reheating process (red curves) follows the tiny oscillations in all cases, again caused by the finite number of trajectories.

In the columns corresponding to the elements of the covariance matrix, we see strong and abrupt changes in the values after the potential switch. The oscillations are larger for the IPP at high pressure and their frequency is two times larger than the oscillation of the particle - as predicted by the theoretical descriptions. In the case of reference measurements (red curves), both position as well as velocity variances increase at high pressure which indicates faster reheating - thermalization of the system to the temperature of the ambient T. On the other hand, at low pressure the reheating over the time of detection is negligible and the variances stay close to 1.

As mentioned above, the thin blue curves in the region of detector dead time are extrapolated data to the time $\bar{t} = \bar{\tau}_2$, i.e. to the moment when the WPP or IPP is switched off and the original harmonic potential is restored. This extrapolation is based on the joint fitting of all 5 quantities by Eqs. (S116–S120) with ($\bar{\mu}_x$,$\bar{\mu}_v$, $\bar{\vartheta}_{xx}$, $\bar{\vartheta}_{vv}$, $\bar{\vartheta}_{xv}$, Ω/Ω_c, Γ, and T/T_0) being the fitted parameters over two periods of particle motion from after recovered signal. The extrapolated curves then follow the evolution given by Eqs. (S116–S120) with the parameters obtained by fitting.

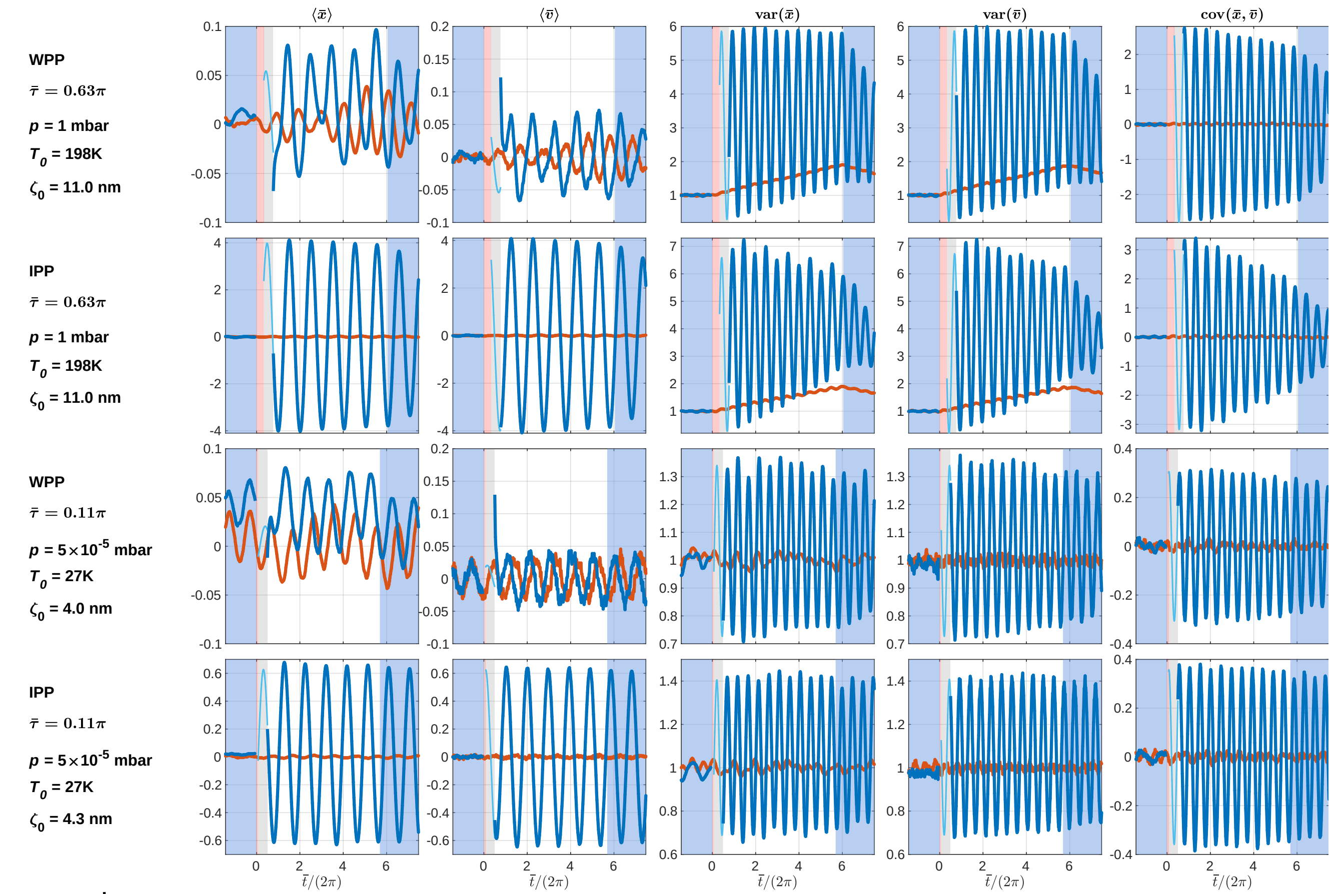

Fig. S13 | Time evolution of the average phase space position, velocity, and covariance matrix. Data were obtained from experimental trajectories under different conditions listed in the first column: Pulse duration $\bar{\tau} \equiv \bar{\tau}_2$, pressure p, initial temperature T_0, and normalization constant $\zeta_0 = \sqrt{\vartheta_{xx}}$ (standard deviation of position). The following columns represent (from left to right) the mean particle position in phase space; the mean velocity in phase space; the phase space variance of particle positions; the phase space variance of particle velocity; the covariance of phase space position and velocity. Blue and red curves compare the behavior of the particle during the potential switch and reference repetitions, respectively. Blue, pink, grey, and white backgrounds depict the period of active cold damping feedback (cooling), potential switch (Step II), detector dead time (recovery), and reading, respectively. Thin parts of the curves (in grey areas) denote regions where the state parameters were extrapolated by fitting the experimental data to analytical equations (S116–S120) for $0 <= \bar{t} - \bar{\tau}_2 < 3\pi$.

S3.2 Squeezed states

Figure S14 shows the time evolution of an extended number of parameters characterizing the squeezing and noise, i.e. major and minor semiaxis of the covariance ellipse $\bar{\sigma}_{\max}$ and $\bar{\sigma}_{\min}$, effective radius $\bar{\sigma}_r$, excess noise δ, non-thermal extension $\bar{\eta}$, ellipticity $\bar{\epsilon}$, and squeezing coefficient λ_{sq} defined above in the theoretical part of SI.

S3.3 Initial state amplification

For an experimental demonstration of the state amplification, we used two measured datasets corresponding to WPP and IPP of the same duration $\tau_2 = 1.8\mu$s. In both cases the initial state was not cooled, i.e. its temperature $T_0 = 300$K and the ambient pressure was 1 mbar. Particle oscillation frequency in the parabolic potential was 130.05 kHz and 131.45 kHz for WPP and IPP with the equilibrium state position standard deviation $\zeta_0 = 14.8$ nm and 15.9 nm, respectively. The WPP and IPP datasets contained 516,000 and 165,000 pairs of reference/switch trajectories, respectively.

S3.3.1 Determination of τ_1 and τ_3 in the Bloch-Messiah transform

In principle, the function of the amplifier can be described as a simple linear transformation

$$\langle \mathbf{x_f} \rangle = \mathbf{G} \langle \mathbf{x_0} \rangle + \mathbf{a}, \tag{S180}$$

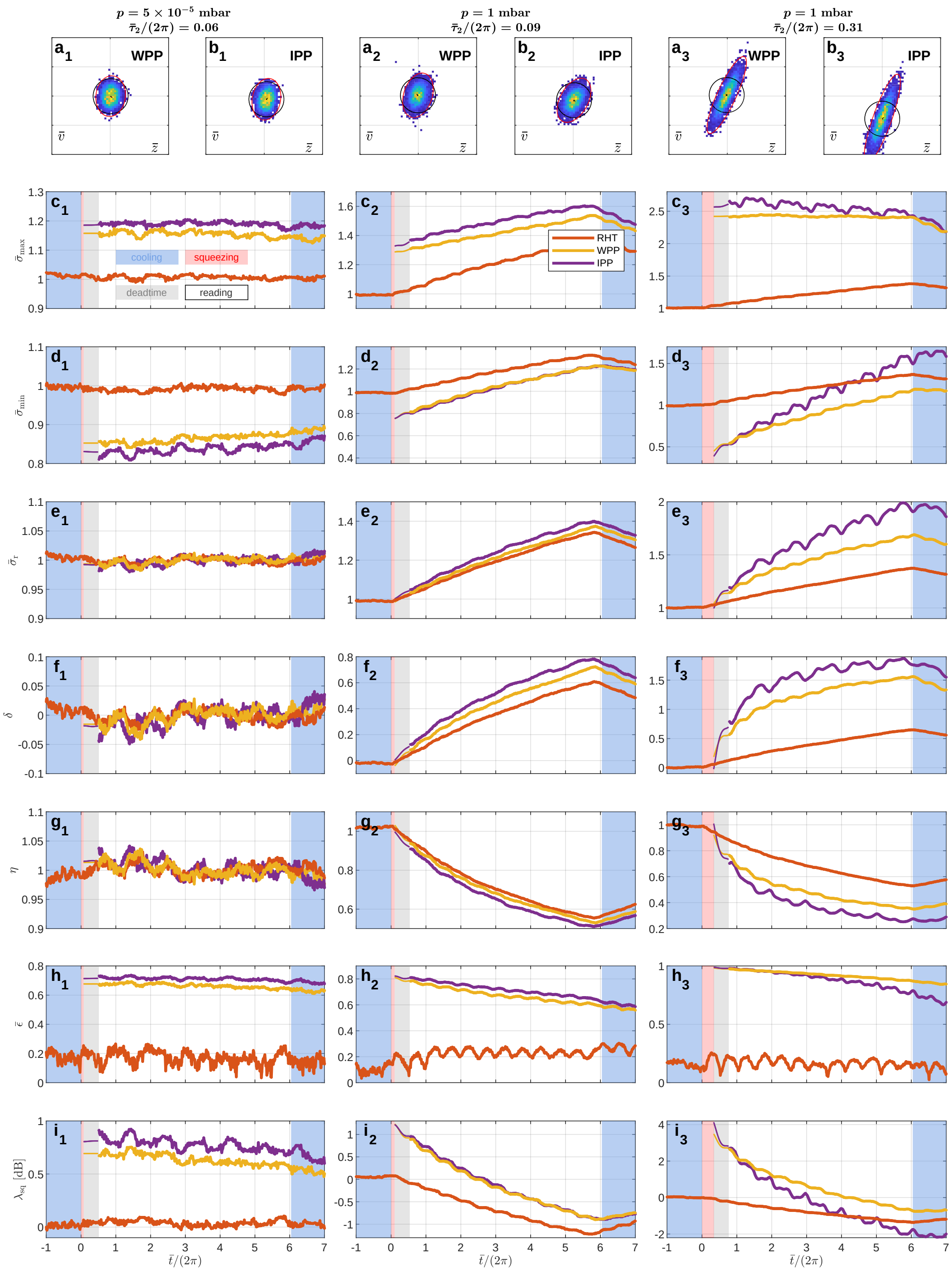

Fig. S14 | Evolution of squeezed state parameters generated by a potential switch to WPP and IPP. $\mathbf{a_1} - \mathbf{b_3}$, experimentally achieved phase space $(x - v)$ distribution of maximally squeezed state obtained at pressure 5×10^{-5} mbar and force pulse duration $\bar{\tau}_2 = 0.06 \times 2\pi$ (columns denoted by subscript $_1$), and 1 mbar for pulsed duration $\bar{\tau}_2 = 0.09 \times 2\pi$ or $0.31 \times 2\pi$ (columns denoted by subscript $_2$ or $_3$, respectively) by WPP (panels **a**) and by IPP (panels **b**). RHT denotes reference conditions with no potential switch. Rows $\mathbf{c_1} - \mathbf{c_3}$, The evolution of the major semi-axis ($\bar{\sigma}_{\max}$). $\mathbf{d_1} - \mathbf{d_3}$, The evolution of the minor semi-axis ($\bar{\sigma}_{\min}$). $\mathbf{e_1} - \mathbf{e_3}$, The evolution of the effective ellipse radius ($\bar{\sigma}_{\mathrm{r}}$). $\mathbf{f_1} - \mathbf{f_3}$, The evolution of excess noise ($\bar{\delta}$). $\mathbf{f_1} - \mathbf{f_3}$, The evolution of non-thermal extension ($\bar{\eta}$). $\mathbf{h_1} - \mathbf{h_3}$, The evolution of the ellipse eccentricity ($\bar{\eta}$). $\mathbf{i_1} - \mathbf{i_3}$, The evolution of the squeezing coefficient (λ_{sq}). Red, yellow, and purple curves depict the behavior of pure reheating (RHT) during the reference condition, WPP, and IPP, respectively. Blue, red, grey, and white areas depict time intervals of active cold damping feedback, potential switch, detector dead time, and reading phase, respectively. Thin parts of curves in grey areas show the state parameters extrapolated by covariance matrix fitting for $\bar{t} - \bar{\tau}_2 < 3\pi$.

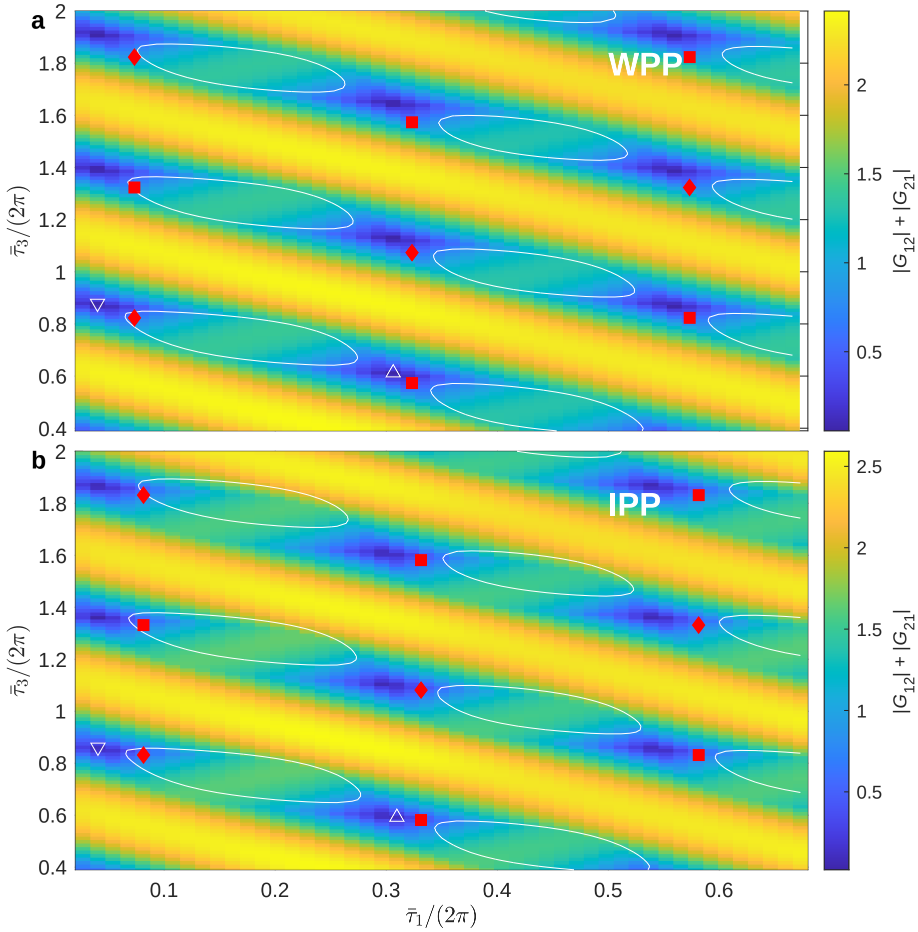

Fig. S15 | Sum of off-diagonal elements of experimental G matrix for different times $\bar{\tau}_1$, $\bar{\tau}_3$. For $|G_{21}|+|G_{12}|=0$ the conditions of the Bloch-Messiah transform are exactly fulfilled. White contours depict points where product of $\mathbf{G}$ matrix diagonal terms $G_{11}G_{22}=1$. Experimental data are shown for amplifier realized by WPP **a** and IPP with the above characterized IPP shift $\bar{\Delta}_c$. White $\triangle$ and $\triangledown$ mark the combinations of $\bar{\tau}_1$, $\bar{\tau}_3$ and $(\bar{\tau}_1', \bar{\tau}_3)'$ where the experimentally obtained values $|G_{21}|+|G_{12}|$ are minimal, respectively. Red squares and diamonds show for comparison $\bar{\tau}_1$, $\bar{\tau}_3$ and $(\bar{\tau}_1', \bar{\tau}_3)'$, respectively, from Eqs. (S156, S157) for experimental parameters.

where $\mathbf{x_0}$ and $\mathbf{x_f}$ are the initial and final phase space positions, $\mathbf{G}$ is 2×2 matrix, and $\mathbf{a}$ is a constant phase space offset caused by additional constant force. Equation (S180) can be used to describe any transformation between final and initial state (assuming linear forces) while the function of the amplifier is obtained only if gain matrix $\mathbf{G}$ non-diagonal elements $G_{12}=G_{21}=0$ and product of diagonal elements $G_{11}G_{22}=1$. The $\mathbf{G}$ matrix depends on times of rotation before pulse $\bar{\tau}_1$, pulse duration $\bar{\tau}_2$, and rotation after pulse $\bar{\tau}_3$, see Supplement S1.7. As the pulse duration is fixed we may select from the acquired trajectories the optimal experimental times $\bar{\tau}_1$ and $\bar{\tau}_3$ that would lead to the elements of $\mathbf{G}$ matrix that are as close as possible to the ideal conditions of the gain matrix.

Therefore, in order to find these times we have to reconstruct the $\mathbf{G}$ matrix. This can be done by the following procedure:

1. Select initial time $\bar{\tau}_1$ prior potential switch
2. Using the procedure in main text Methods we generate 100 trajectories that originate at a given phase space position $(\bar{\mu}_x, \bar{\mu}_v)$.
3. We generate in total 749 of such trajectory ensembles for various initial positions fulfilling $\bar{\mu}_{x,i}^2+\bar{\mu}_{v,i0}^2\leq 1.5^2$. Thus, we obtain 749 of initial phase space mean positions $\mathbf{x}_{\mathbf{0},i}(\bar{\tau}_1)$.
4. For given time after pulse $\bar{\tau}_3$ calculate the final phase space positions $\mathbf{x_f}(\bar{\tau}_1,\bar{\tau}_3)$.
5. Perform least-squares fitting to find optimal values of $\mathbf{G}$ matrix and $\mathbf{a}$ vector elements. In the case of WPP only the elements of $\mathbf{G}$ are searched for.

6. Repeat the procedure above for different times $\bar{\tau}_1$ and $\bar{\tau}_3$

Figure S15 shows the sum of $\mathbf{G}$ matrix off-diagonal elements absolute values $|G_{21}| + |G_{12}|$ in the form of color maps for both WPP and IPP for various combination of times $\bar{\tau}_1$ and $\bar{\tau}_3$. For some of the combinations, $|G_{21}|+|G_{12}|$ gets close to zero but never reaches exact zero. White contours in Fig. S15 mark the combinations of $\bar{\tau}_1$ and $\bar{\tau}_3$ where the experimental diagonal elements satisfy $G_{11}G_{22} = 1$ (and $G_{11}G_{22} > 1$ outside them). These white contours, however, do not reach the triangles with minimal $|G_{21}|+|G_{12}|$. This indicates, the experimentally obtained amplifications would amplify one phase space coordinate but the squeezing of the other one would be weaker than predicted by Bloch-Messiah transformation. Furthermore, the red squares and diamonds show the solutions of Eqs. (S156, S157) for given experimental parameters, squares correspond to solution $(\bar{\tau}_1, \bar{\tau}_3)$ and diamonds to $(\bar{\tau}_1', \bar{\tau}_3)'$, respectively. We can see, the red squares and diamonds marking the solutions of Eqs. (S156, S157), are closer to the white contours and are slightly displaced towards bigger values of $\bar{\tau}_1$ and smaller values of $\bar{\tau}_3$. This is most likely caused by the reheating process that occurs between the initial state in $\bar{t} = 0$ and final time $\bar{t}_f$ at the experimental pressure 1 mbar. The reheating will break down the symplectic property of the matrix $\mathbf{G}$, i.e. its determinant no longer equals to 1, and the exact conditions of the Bloch-Messiah theorem could not be fulfilled. For further analysis, we selected combinations of $\bar{\tau}_1$ and $\bar{\tau}_3$, marked by $\triangle$ and $\triangledown$ in Fig. S15, that lead to optimal amplification of position and velocity, respectively, with minimal crosstalk between position and velocity phase space coordinates.

S3.3.2 Amplification of mean values

Figure 2a-d of the main text demonstrates the position and/or velocity amplification of the mean positions by a set of colored arrows. Here, we will quantify in greater detail the difference between the idealized function of the force pulse amplifier and the measured data. We will focus on the amplification of position and velocity obtained by WPP, see Fig. 2a,b in the main text, that are characterized by the experimental $\mathbf{G_e}$ matrices

$$\mathbf{G_{e,x}} = \begin{pmatrix} 1.867\pm0.003 & 0.004\pm0.003 \\ -0.052\pm0.003 & 0.484\pm0.003 \end{pmatrix}, \tag{S181}$$

$$\mathbf{G_{e,v}} = \begin{pmatrix} 0.502\pm0.004 & 0.100\pm0.003 \\ -0.006\pm0.004 & 1.882\pm0.003 \end{pmatrix}. \tag{S182}$$

The errors of the values represent 95% confidence interval of the linear regression fits.

Figure S16a, b, e, f shows the transformations of the initial mean phase space coordinates $\langle \mathbf{x}_0 \rangle$ to the final phase space coordinates $\langle \mathbf{x}_f \rangle$, found from the experimental trajectories as we described above. These figures extend results of main text Figs. 2a,c that show the same coordinate transformation only for a few initial points as displacement vectors. Panels c,d,g,h of Fig. S16 depict the relative errors $\delta\bar{x}$ and $\delta\bar{v}$ between the experimental final phase space positions and the final phase space positions predicted by $\mathbf{G}_e$ matrices, i.e.

$$\delta\bar{x} = \frac{\bar{x}_{e,f} - (G_{11}\bar{\mu}_{xe} + G_{12}\bar{\mu}_{ve})}{G_{11}\bar{\mu}_{xe} + G_{12}\bar{\mu}_{ve}}, \tag{S183}$$

$$\delta\bar{v} = \frac{\bar{v}_{e,f} - (G_{21}\bar{\mu}_{xe} + G_{22}\bar{\mu}_{ve})}{G_{21}\bar{\mu}_{xe} + G_{22}\bar{\mu}_{ve}} \tag{S184}$$

Figures S16a, c, f, h show that the amplified coordinate (x in panels a, c and v in panels f, h) follow very well linear transformation by the appropriate elements of $\mathbf{G_e}$ matrices with deviation $\delta\bar{x}$ or $\delta\bar{v}$ smaller than 10%. On the other hand, stronger non-linear effects of the 3rd order are seen in the complementary coordinate that should be squeezed, see Fig. S16b,e. This leads to up to 50% relative deviations $\delta\bar{x}$ or $\delta\bar{v}$. This relative difference is the strongest close to the points where the predicted squeezing is close to zero, while farther away the difference gets smaller than 10%. Such non-linear effects are related to the sinusoidal profile of the force acting both before, during, and after the force pulse. Their effect may be suppressed by considering a cooled initial state at lower pressure where the particle motion is localized closer to the parabolic bottom of the periodic potential and does not reach the non-linear region.

S3.4 Noise amplification

Let us now consider an amplification of an initial state that is normally distributed with phase space mean $\bar{\mathbf{x}}_\mathbf{0} = (\bar{\mu}_x, \bar{\mu}_v)$ and covariance matrix $\mathbf{\Theta}$. If we consider an amplification sequence characterized by the matrix $\mathbf{G}$ (assuming no potential displacement $\Delta_c = 0$), the final state mean values and covariance are the following

$$\langle \bar{\mathbf{x}}_\mathbf{f} \rangle = \mathbf{G}\bar{\mathbf{x}}_\mathbf{0}, \tag{S185}$$

$$\mathbf{\Theta_f} = \mathbf{G}\mathbf{\Theta}\mathbf{G}^T. \tag{S186}$$

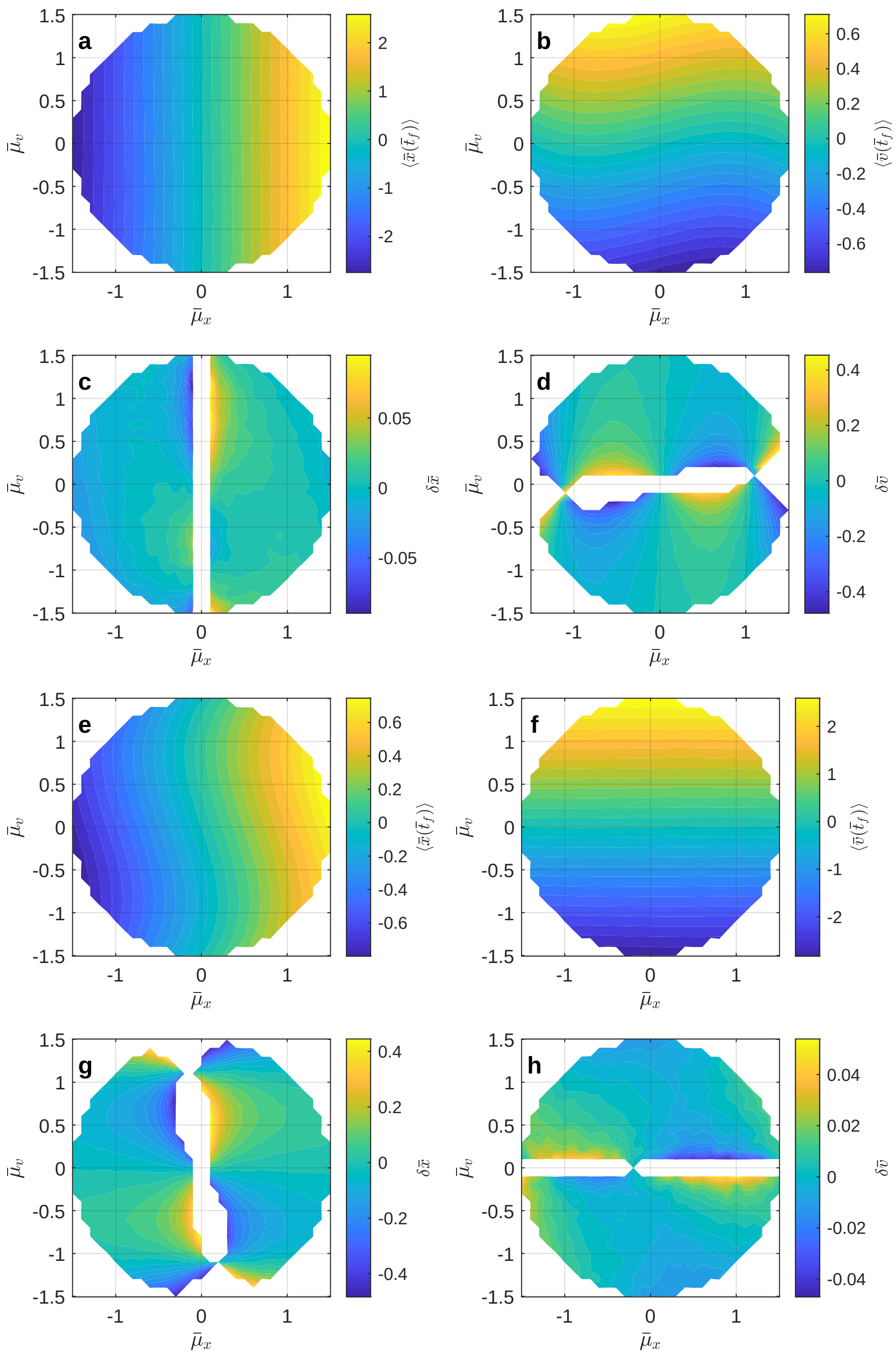

Fig. S16 | Experimentally observed transformation from the initial noise-less phase space coordinates $\langle \mathbf{x}_0 \rangle$ to the final coordinate $\langle \mathbf{x}_f \rangle$. a-d, Focus on the amplification of position given by matrix Eq. (S181) and, **e-h**, deal with the amplification of velocity amplification given by matrix Eq. (S182). **a**, For the selected initial mean values of position and velocity (a single point in the phase space plot) $\mathbf{x}_0 \equiv (\bar{\mu}_x, \bar{\mu}_v)^T$ the color encodes the final value of the mean position $\langle \bar{x}_f \rangle$ for this initial point. **b**, Similar plot as **a** but the color encodes the final value of the mean velocity $\langle \bar{v}_f \rangle$. **c**, The color encodes the difference between $\langle \bar{x}_f \rangle$, obtained in **a**, and the value $\langle \bar{x}_f \rangle$ obtained from the Eqs. (S181) using the linear transform (S180) (see Eq. S183). **d**, The same as **c** but using Eq. (S184). Results presented in **e-g** are equivalent to **a-d** but for the gain matrix given by Eq. (S182) amplifying velocity.

In the ideal case of diagonal $\mathbf{G}$ matrix with reciprocal diagonal elements the amplified noise variance would amplify/squeeze the diagonal elements of the covariance matrix only as

$$\mathbf{\Theta_f} = \begin{pmatrix} \vartheta_{xx}G^2 & \vartheta_{xv} \\ \vartheta_{xv} & \vartheta_{vv}/G^2 \end{pmatrix}. \tag{S187}$$

However, if the experimental case $\mathbf{G}$ matrix contains small (but non-negligible) off-diagonal elements and the on-diagonal elements are not exactly reciprocal, we will obtain for the covariance matrix amplification

$$\mathbf{\Theta_f} = \begin{pmatrix} \vartheta_{xx}G_{11}^2 + 2\vartheta_{xv}G_{11}G_{12} & \vartheta_{xv}G_{11}G_{22} + \vartheta_{xx}G_{11}G_{21} + \vartheta_{vv}G_{12}G_{22} \\ \vartheta_{xv}G_{11}G_{22} + \vartheta_{xx}G_{11}G_{21} + \vartheta_{vv}G_{12}G_{22} & \vartheta_{vv}G_{22}^2 + 2\vartheta_{xv}G_{22}G21 \end{pmatrix}. \tag{S188}$$

Here we assumed that the quadratic products of the off-diagonal $\mathbf{G}$ matrix elements (G_{12}^2, G_{21}^2, $G_{12}G_{21}$) are negligible. In this case the amplification of $\bar{\theta}_{xx}$ and $\bar{\theta}_{vv}$ elements of the covariance matrix would also contain contributions of the initial noise correlation $\bar{\vartheta}_{xv}$ and the final state correlation would also contain contributions of the initial state noise in both x and v.

In order to study the amplification of normally distributed (noisy) initial states we generated the initial distribution of points using the procedure given in the Methods part of the main text. We considered the same phase space initial mean positions $\mathbf{x_0}$ as in Fig. S16 but we added a "thermal-like" initial state characterized by the diagonal covariance matrix $\mathbf{\Theta} = \vartheta_0\mathbf{I}$, where ϑ_0 is the initial state variance and $\mathbf{I}$ is the 2×2 unit matrix. Thus we get a set of experimental trajectories with given initial properties. Using the same procedure as above we found the gain matrix with minimal $|G_{21}| + |G_{12}|$ for each level of initial noise.

As expected the final state mean and covariance do depend only on the corresponding initial moments. Figure S17a and b compare the final state amplification in x axis assuming two initial variances $\bar{\vartheta}_0 = 0.01$ and 0.1. Their differences are shown in Fig. S17c and demonstrate that the mean positions almost do not depend on the initial variances. Further, the average amplification of the initial state position in x axis $\langle G_{11}\rangle$ and squeezing in v axis $\langle G_{22}\rangle$ for various amounts on initial noise variance is shown in Fig. S17d and e as blue curves having an error depicted as a blue band. Within the "error-bars" the position amplification curves is almost constant for small strengths of the input noise and slightly decrease for input noise $\vartheta_0 > 0.1$ and it is constant for velocity squeezing. The tiny decrease of G_{11} (blue curve in S17d) with increasing input noise is caused by the PSPD of the final state that deviate from ideal Gaussian due to weak nonlinear force components that influence mostly stochastic trajectories with big phase space amplitudes. Yet, one should note that this change is in the order of one percent. Moreover, the values of G_{11} and G_{22} given in Eq. (S181) are plotted as red dashed lines with their errors depicted by red bands. We can see very good match of both diagonal elements (G_{11}, G_{22}) obtained for both methods based on Gaussian initial PSPDs (blue) and "zero variance" ones (red).

As in Fig. 2h of the main text, figure S17f demonstrates the amplification of the initial Gaussian state (blue color map) characterized by the initial variance $\vartheta_0 = 0.1$ to the amplified state (green color map). Furthermore, Figs. S17g and h show that the amplified final state variance $\bar{\theta}_{xx}$ only weakly depends on the initial mean positions for two different initial variance levels of $\vartheta_0 = 0.01$ and 0.1 (panels g and h, respectively). In principle, the observed $\bar{\theta}_{xx}$ should not depend on the initial mean phase space position at all, see Eq. (S186). The variations of experimental $\bar{\theta}_{xx}$ appear as the initial phase space position gets farther away from zero it is most likely caused by the non-linear force terms.

The amplified variance $\bar{\theta}_{xx}$, averaged over all initial phase space mean positions, is plotted as blue dots in Fig. S17i for a broad range of initial variance ϑ_0. It increases linearly as expected from Eq. (S186). The red line shows the predicted variance using the value of G_{11} from Eq. (S181). The vertical offset between both curves is caused by the reheating process that is not included in the simple model. Figure S17j shows the dependence of the variance θ_{vv} for the same conditions as θ_{xx} in the previous panel. The linear increase in the measured variance is visible as well.

Figure S17k and l show the input (k) and output (l) signal-to-noise ratio (SNR_i and $\mathrm{SNR}_o^{(x/v)}$) of position and velocity, i.e.

$$\mathrm{SNR}_i^{(x)}(\bar{\mu}_x, \bar{\vartheta}_0) = \frac{\langle\mu_x\rangle_v^2}{\bar{\vartheta}_0}, \tag{S189}$$

$$\mathrm{SNR}_o^{(x)}(\bar{\mu}_x, \bar{\vartheta}_0) = \frac{\langle x_f\rangle_v^2}{\langle\bar{\theta}_{xx}\rangle_v}, \tag{S190}$$

and similarly for velocities. $\langle\cdot\rangle_v$ means the average taken over all realizations of the given quantity for various velocities v. This practically means, we evaluated numerically SNR for all combinations of the input mean values in

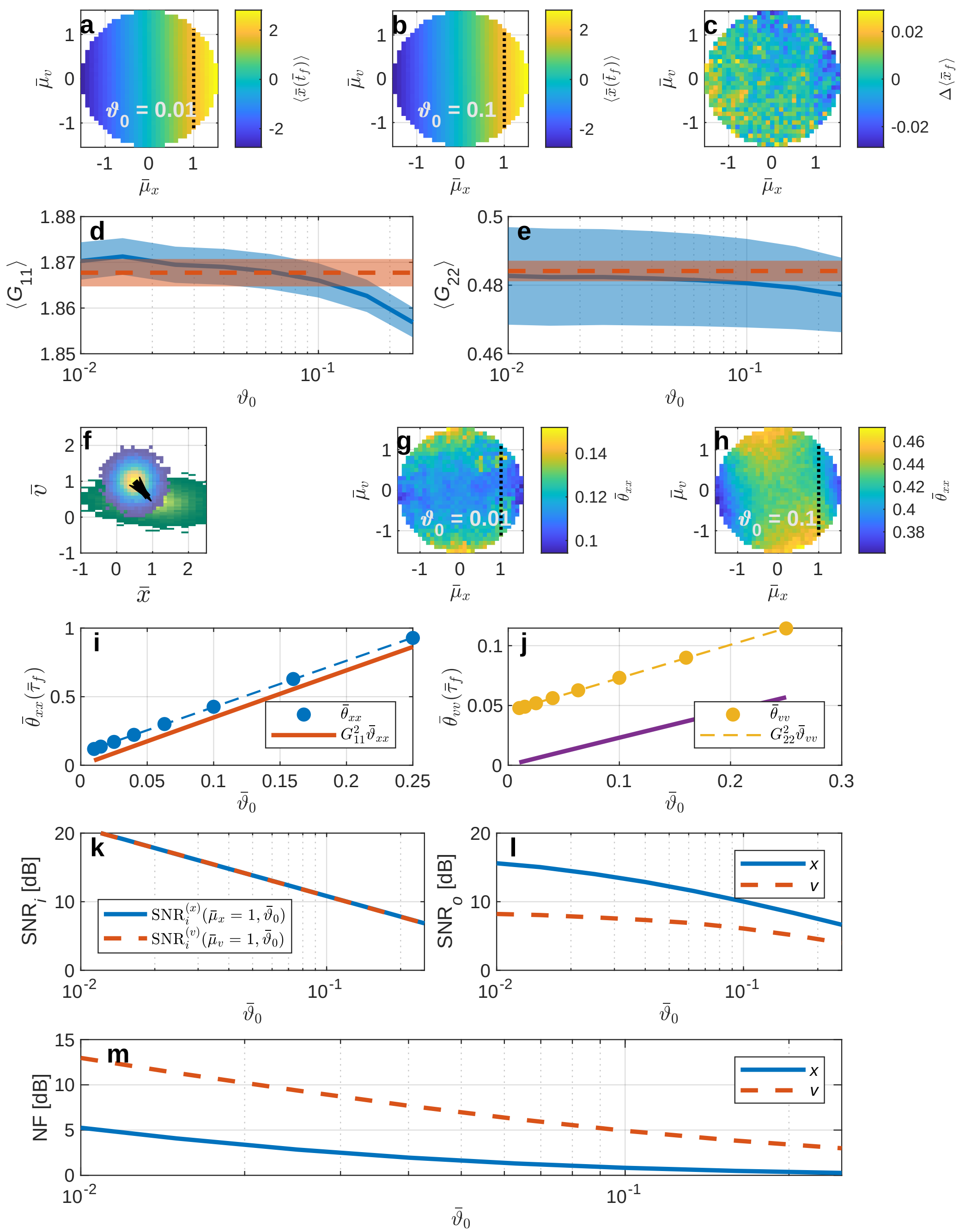

Fig. S17 | Properties of the amplification of initial states with Gaussian noise. a-b, Mean values of the final state amplified in position x assuming two initial variances (initial noise) $\bar{\vartheta}_0 = 0.01$ (**a**) and 0.1 (**b**), respectively. **c**, The difference of the amplified positions $\Delta\langle x_f\rangle = \langle x_f\rangle_{\bar{\vartheta}_0=0.01} - \langle x_f\rangle_{\bar{\vartheta}_0=0.1}$ in panels **b** and **a**. **d-e**, Dependence of the mean value of G_{11} and G_{22} on the initial variance $\bar{\vartheta}_0$ (blue curves). The values of G_{11} and G_{22} given in Eq. (S181) are plotted as the red dashed lines. **f**, Experimental demonstration of amplification of the initial noisy states (blue maps) by the WPP to the final state (green maps). The panel corresponds to Fig. 2h of the main text. **g,h**, $\bar{\theta}_{xx}$ component of the amplified state covariance matrix for various mean initial phase space positions and 2 levels of the initial variance $\vartheta_0 = 0.01$ (panel **g**) and $\vartheta_0 = 0.1$ (panel **h**). **i**, Position variance $\bar{\theta}_{xx}$ amplification (blue dots) for different amounts of initial variance ϑ_0. The red line shows the noise amplification predicted by the diagonal elements of the ideal **G** matrix. **j**, Velocity variance $\bar{\theta}_{vv}$ squeezing (yellow dots) for different amounts of initial variance ϑ_0. The purple line shows the noise level predicted by diagonal elements of the ideal **G** matrix. Note a different scale compared to **i**. **k-l**, Input (**k**) and output (**l**) signal-to-noise ratios (SNR) of position (blue) and velocity (red, dashed) coordinates calculated for $\mu_x = 1$ (position SNR) and for $\mu_v = 1$ (velocity SNR), respectively. Output position $\mathrm{SNR}_o^{(x)}$ for input noise levels $\bar{\vartheta}_0 = 0.015, 0.1$ was calculated amplified output signal and noise along the vertical dotted lines in panels **a,b,g,h**. **m**, Noise figure (NF) of the amplifier as a function of the input noise ϑ_0.

position and velocity μ_x, and μ_v, and for all levels of the input noise $\bar{\vartheta}_0$. In principle, the SNR of position (velocity) in linear system without cross-talks should depend only on the input signal of position (velocity), i.e. the SNR of position (velocity) is a function of the mean input value, μ_x or μ_v for $\mathrm{SNR}_{i,o}^{(x)}$ $\mathrm{SNR}_{i,o}^{(v)}$, respectively. Therefore, we performed the "marginalization" (averaging) over the complementary coordinate. This could be seen for output position $\mathrm{SNR}_o^{(x)}$ two levels of input noise in Figs. S17a,b,g,h. The vertical black dotted line shows the output signal x_f that is independent on v as well as the output noise $\bar{\theta}_{xx}$ which is only weakly position dependent. Figure S17k shows that the input SNR decreases as $1/\bar{\vartheta}_0$ as expected due to the increase of input noise. However, in the case of output SNR (Fig.S17l the dependence on the input noise level changes due to the presence of internal amplifier noise caused by the reheating. The reheating influences most strongly the output SNR of the smallest input noise where the biggest change between input and output SNR is visible.

Both SNRs are used to calculate the noise figure (NF) of signal amplification

$$\mathrm{NF}(\vartheta_0) = \left\langle \frac{\mathrm{SNR}_i}{\mathrm{SNR}_o} \right\rangle_x . \tag{S191}$$

Assuming that both signal squared as well as noise variance scale in the amplification process by simple factor G^2 the noise figure can be easily expressed as

$$\mathrm{NF} = 1 + \frac{N_a}{G^2 \vartheta_0}, \tag{S192}$$

where N_a denotes the noised added during the amplification process, i.e. in our case the thermal reheating. NF for various levels of input noise is plotted in see Fig. S17m. One can see that due to the presence of reheating, i.e. in an analogy with the electronic amplifier noise, leads to high values of NF ~ 5 dB for high input SNR_i. In such a case the output noise is dominated by the noise of the amplification process itself. Only when the input noise level increases above $\vartheta_0 > 0.1$ the input SNR_i decreases and NF gets bellow 1 dB and the output noise contain only $\sim$ 20% of the noise generated internally in the amplification process.